PREPRINT SUBMITTED

This manuscript is a **preprint** uploaded to **EarthArXiv**. The first version of this preprint has been submitted for publication to Tectonics on the 24th of January 2022. Authors encourage downloading the latest manuscript version from EarthArXiv, and welcome comments, feedback and discussions anytime.

Please, feel free to get in contact: gino@ginodegelder.nl

Quaternary E-W extension uplifts Kythira Island and segments the Hellenic Arc

G. de Gelder[1,2], D. Fernández-Blanco[2,3], N. Öğretmen[4,5], S. Liakopoulos[6], D. Papanastassiou[6], C. Faranda[5], R. Armijo[2], and R. Lacassin[2]

[1]ISTerre, Université Grenoble-Alpes, 1381 Rue de la Piscine, 38400 St. Martin d'Hères, France

[2]Université de Paris, Institut de physique du globe de Paris, CNRS, F-75005 Paris, France

[3]Barcelona Center for Subsurface Imaging, Passeig Marítim de Barceloneta 37-49, E-08003 Barcelona, Spain

[4]Eurasia Institute of Earth Sciences, Istanbul Technical University, 34467, Istanbul, Turkey

[5]Dipartimento di Scienze, Università degli Studi Roma Tre, Largo San Leonardo Murialdo, 1, 00146 Rome, Italy

[6]Institute of Geodynamics, National Observatory of Athens, GR-11810 Athens, Greece

Corresponding author: Gino de Gelder (gino.de-gelder@univ-grenoble-alpes.fr)

Key Points:

- ~100 m of Tortonian-Pliocene subsidence of Kythira Island was followed by ~300-400 m of uplift since ~2.6 Ma.
- Regional E-W extension, caused by large-scale plate boundary changes ~1.5-0.7 Ma, is uplifting Kythira Island.
- We highlight the general importance of upper crustal faulting as a major driver of forearc uplift.

Abstract

Several crustal and lithospheric mechanisms lead to deformation and vertical motion of the upper plate during subduction, but their relative contribution is often enigmatic. The Hellenic Forearc has been uplifting since Plio-Quaternary times, yet the spatiotemporal characteristics and sources of this uplift are poorly resolved. The remarkable geology and geomorphology of Kythira Island, in the southwestern Hellenic forearc, allow for a detailed tectonic reconstruction since the Late Miocene. We present a morphotectonic map of the island, together with new biostratigraphic dating and detailed analyses of active fault strikes and marine terraces. We find that the Tortonian-Pliocene stratigraphy in Kythira records ~100 m of subsidence, and a wide coastal rasa marks the ~2.8-2.4 Ma maximum transgression. Subsequent marine regression of ~300-400 m and minor E-W tilt are recorded in ~12 marine terrace levels at uplift rates of ~0.2-0.4 mm/yr. Guided by simple landscape evolution models, we interpret the coastal morphology as the result of initial stability or of slow, gradual sea-level drop since ~2.8-2.4 Ma, followed by faster uplift since ~1.5-0.7 Ma caused by roughly N-S normal faulting. Our findings on- and offshore emphasize that E-W extension is the dominant mode of regional active upper crustal deformation, and N-S normal faults accommodate most, if not all of the uplift on Kythira. We interpret the initiation of E-W extension as the result of a change in plate boundary conditions, in response to either propagation of the North Anatolian Fault, incipient collision with the African plate, mantle dynamics or a combination thereof.

1 Introduction

The mode of deformation of the upper plate during subduction and the mechanisms of uplift at the front of the overriding plates are two fundamental questions largely addressed that remain unresolved (e.g. Davis et al., 1983; Willet et al., 1993; Larroque et al., 1995; Gutscher et al., 1996; Fuller et al., 2006; Gallen et al., 2014). The Hellenic subduction assumes the largest convergence velocity and holds the highest seismic activity among Mediterranean arcs (McClusky et al., 2000; Reilinger et al., 2006), and thus, its forearc is key in this debate. The steep normal faults that control the present-day structuration and seismicity of the Hellenic Arc are oblique to the intraplate contact and change in orientation along the arc, transecting former fold-and-thrust structures that are parallel to the trench (Lyon-Caen et al., 1988; Armijo et al., 1992; de Chabalier et al., 1992; Shaw and Jackson, 2010). Constraining the timing and kinematics of these normal faults, and of the recent structuration of the arc between uplifted islands and offshore grabens, is of prime relevancy to better understand the mechanics of the Hellenic plate boundary.

Kythira is the largest island between SW Peloponnese and NE Crete (Fig. 1), and provides an exceptional but surprisingly unattended opportunity to understand the interaction between past and active tectonics in the Hellenic Arc. Kythira's sedimentary record and morphological characteristics allow a detailed reconstruction of its tectonic evolution since the Late Miocene. Whereas emerged marine sedimentary basins record the island vertical motions during the Neogene, its landscape archives a recent uplift phase as coastline abrasion surfaces, marine terraces and steep river gorges. Holocene fault scarps and numerous historical earthquakes (Papadopoulos and Vassilopoulou, 2001) evidence active faulting, but controversy remains on the processes that drove the initiation of the main fault systems, both on the island itself and within the regional context of the Hellenic Arc.

We reconstruct the Late Miocene-Recent tectonic evolution of Kythira through a multi-disciplinary approach that includes morphometric and basin analyses, fieldwork, biostratigraphic dating and numerical modeling. We developed a 2 m-resolution Digital Surface Model (DSM) from Pleiades satellite imagery that allows us to detect and map geologic and geomorphic features like faults, marine terraces, drainage systems and stratigraphic layering with unprecedented detail. We present a detailed geological, structural and geomorphological map of Kythira Island, and a comprehensive analysis of marine terraces based on a combination of fieldwork and the high resolution DSM. We constrain absolute ages and evaluate the rates of surface uplift dating marine deposits near the highest and most extensive marine abrasion surface of the island with microfossils. Combining these ages and the coastal morphology, we then use simple landscape evolution models to test different uplift scenarios. This allows us to put forward a detailed discussion on the tectonic changes that have affected the island, and discuss our findings in the context of the evolution of the Hellenic Arc.

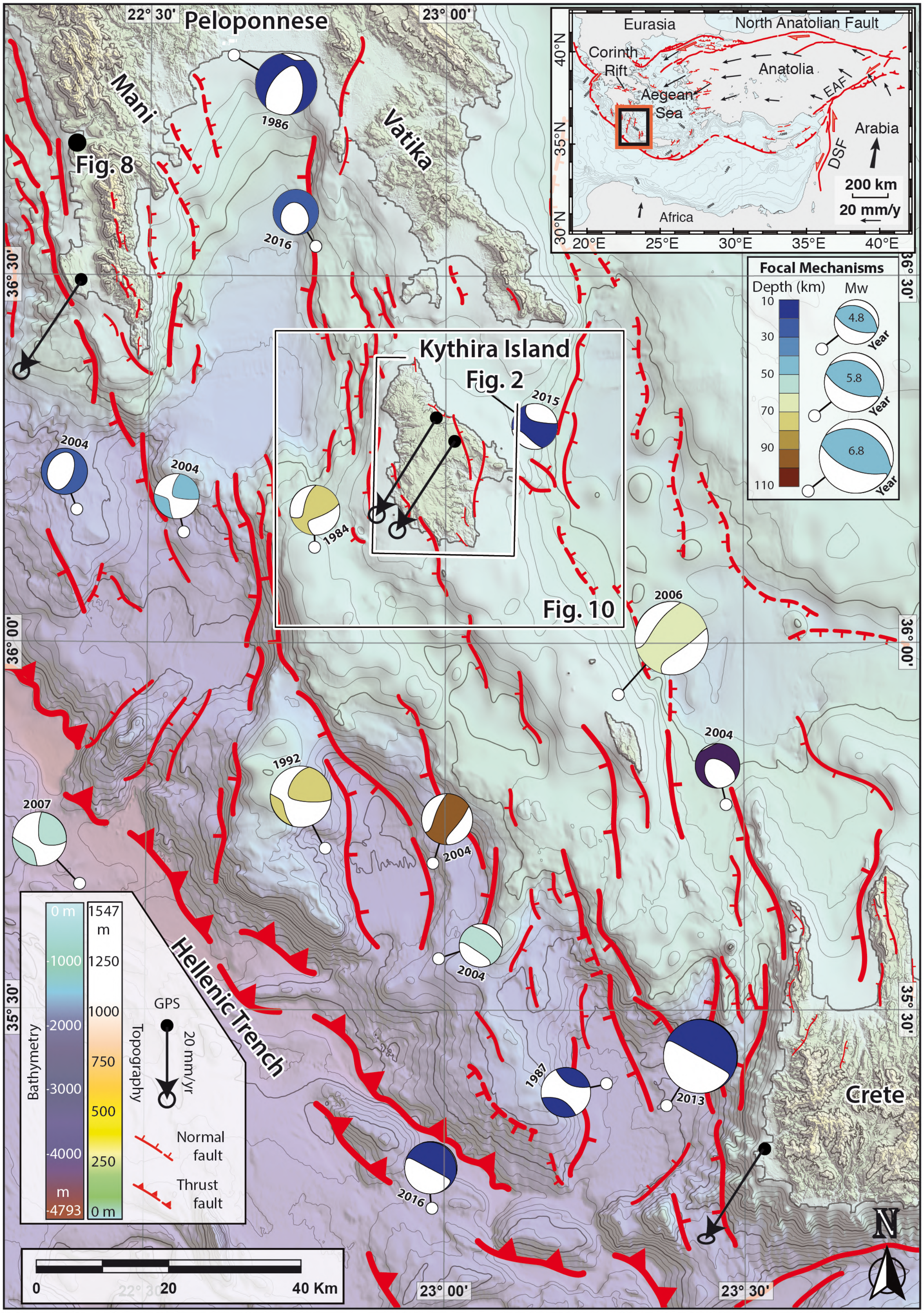

Peloponnese
Mani
Vatika
Fig. 8
Kythira Island
Fig. 2
Fig. 10
Hellenic Trench
Crete
Eurasia
North Anatolian Fault
Corinth Rift
Anatolia
Aegean Sea
EAF
Arabia
DSF
Africa
200 km
20 mm/y
Focal Mechanisms
Depth (km)
Mw
Year
Bathymetry
Topography
GPS
20 mm/yr
Normal fault
Thrust fault
0
20
40 Km

Figure 1*. *Active tectonics of the SW Hellenic Arc. *Topography is an ALOS Global Digital Surface Model (DSM), and bathymetry is from the European Marine Observation and Data Network (EMODNet) Digital Terrain Model (DTM). Offshore fault mapping is an interpretation of the bathymetry based on relief offset and morphology, and accounts for fault mapping by Lyberis et al. (1982) and Armijo et al. (1992). Focal mechanisms (>4.5 Mw since 1976, colored by depth and sized by magnitude) are build using both the main and the monthly-curated databases of the Global Centroid Moment Tensor (GCMT) catalog (https://www.globalcmt.org/; Ekström et al., 2012), as downloaded on the 14th December 2020. GPS vectors are relative to stable Eurasia, and taken from England et al. (2016), but we note that these would be similar in direction and magnitude if re-calculated with respect to stable Nubia (Reilinger et al., 2006; Shaw and Jackson, 2010). The location of figures 2, 8 and 10 is indicated.*

2 Tectonic, geologic, and geomorphic setting

Subduction of the African plate below the Aegean has stacked the Hellenic fold-and-thrust belt nappes since the early Mesozoic (e.g. Aubouin, 1957; Jacobshagen, 1986; Facenna et al., 2003; van Hinsbergen et al., 2005; Jolivet and Brun, 2010). Three of those nappes are exposed on Kythira: the Arna Unit, the Tripolis Unit and the Pindos Unit (Manolessos, 1955; Papanikolaou and Danamos, 1991; Danamos, 1992). The HP/LT metamorphic Arna Unit (Gerolymatos, 1994; Marsellos and Kidd, 2008; Marsellos et al., 2014) is highly folded and crops out in the north of the island. Overthrusting the Arna Unit, the Tripolis Unit contains Jurassic-Eocene limestones, dolomites and flysch (Danamos, 1992). The Tripolis Unit crops out along large parts of the NE and SW coasts and in the center of the island, typically along NW-SE trending ridges parallel to the Hellenic trench. The Pindos Unit overthrusts both underlying units and contains Cretaceous-Early Cenozoic limestones and flysch (Danamos, 1992). It mainly crops out in the central and SE parts of the island, and has a NW-SE trend similar to the Tripolis Unit. Apatite and zircon fission track cooling ages for the metamorphic Arna Unit indicate exhumation during the Middle-Late Miocene (Marsellos and Kidd, 2008; Marsellos et al., 2014). The oldest preserved Neogene sediments on Kythira Island are of Tortonian age (Theodoropoulos, 1973; Meulenkamp et al., 1977; van Hinsbergen et al., 2006), and were probably deposited not long after exhumation ceased.

Neogene-Quaternary rocks unconformably overlie the Hellenic nappes and are scattered around the island, with the largest basin located in its central-eastern sector, between Potamos and Avlemonas (Fig. 2). The Neogene stratigraphy has previously been described as a Tortonian terrigenous-clastic succession at the bottom overlaid in angular unconformity by a Pliocene calcareous succession (Theodoropoulos, 1973; Meulenkamp et al., 1977). Paleobathymetry estimates from a Plio-Pleistocene calcareous section near the present-day coast at Avlemonas (orange star on Fig. 2) suggest deepening from ~300 to ~750 m depth between ~3.5 and ~2.5 Ma (van Hinsbergen et al., 2006).

The highest elevated sediments of the calcareous succession form part of a large marine rasa (Fig. 2), i.e. a wide coastal planation surface of polygenic origin formed by sea erosion during multiple sea-level stands (e.g. Guilcher, 1974; Pedoja et al., 2006; Regard et al., 2010; Dawson et al., 2013). The rasa in Kythira is carved into both basement nappes and Neogene sediments (Fig. 2), is most extensive around the airport (NE of Mitata), and can be found all around the island between elevations of ~200 and ~400 m. It forms the highest marine abrasion surface in a flight of marine terraces that reaches the present-day coastline, which is best preserved along the east coast. Gaki-Papanastassiou et al. (2011) described 6-8 different terrace levels in the southern part of the island, with sea caves and notches at 0.4-0.6, 2, and 4 meters above sea level evidencing recent uplift.

The active faults on the island have been described as a combination of NW-SE and NE-SW trending normal faults related to trench-normal and trench-parallel extension respectively (Marsellos and Kidd, 2008), or NNW-SSE trending normal faults related to N-NE directed subduction (Gaki-Papanastassiou et al., 2011). Historical earthquakes in Kythira have been documented in 800 AD, 1750, 1798, 1866 and 1903 (Gaki-Papanastassiou et al., 2011), but are difficult to associate with specific faults. The 2006 magnitude 6.7 Mw earthquake that caused significant destruction to the town of Mitata (Fig. 2) had a focal depth of ~60 km (Fig. 1), and is thus probably unrelated to any of the faults observed on the island (Konstantinou et al., 2006).

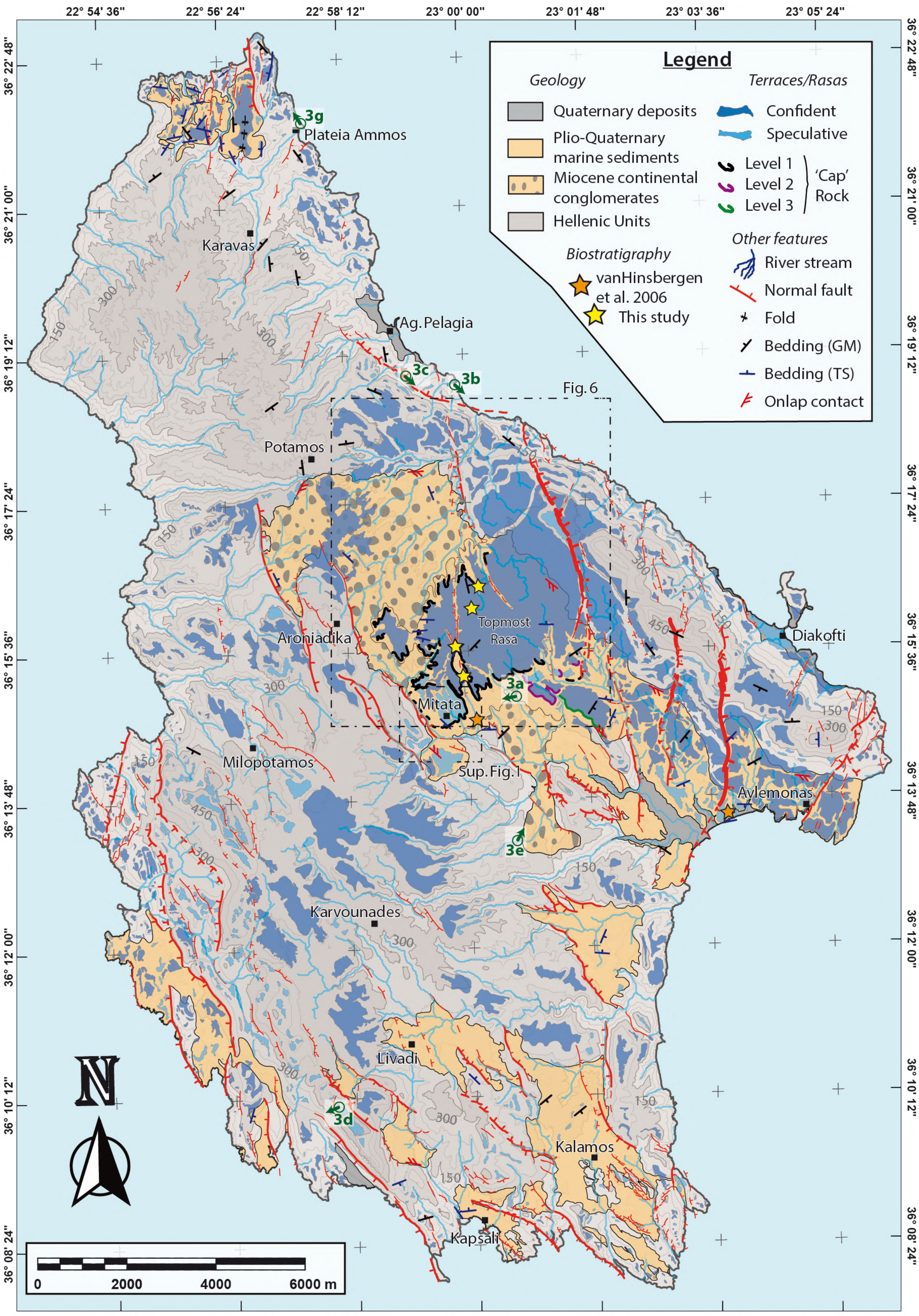
Legend
Geology
Quaternary deposits
Plio-Quaternary marine sediments
Miocene continental conglomerates
Hellenic Units
Terraces/Rasas
Confident
Speculative
Level 1
Level 2
Level 3
'Cap' Rock
Biostratigraphy
vanHinsbergen et al. 2006
This study
Other features
River stream
Normal fault
Fold
Bedding (GM)
Bedding (TS)
Onlap contact
Plateia Ammos
Karavas
Ag. Pelagia
Potamos
Aroniadika
Topmost Rasa
Mitata
Milopotamos
Diakofti
Avlemonas
Karvounades
Livadi
Kalamos
Kapsali
Fig. 6
Sup. Fig. 1
3a
3b
3c
3d
3e
3g
0
2000
4000
6000 m
22° 54' 36''
22° 56' 24''
22° 58' 12''
23° 00' 00''
23° 01' 48''
23° 03' 36''
23° 05' 24''
36° 22' 48''
36° 21' 00''
36° 19' 12''
36° 17' 24''
36° 15' 36''
36° 13' 48''
36° 12' 00''
36° 10' 12''
36° 08' 24''

133

Figure 2*. *Active tectonics on Kythira. *Map with main geologic and geomorphic features, based on 2m-resolution Digital Surface Model developed from Pleiades satellite imagery and fieldwork (see text). Topographic contours are given at 50 m intervals, with color changes every 150 m. Active faults in red have different stroke thickness to show 5 levels of relative offset, and most present fault scarps as corroborated in situ during fieldwork. Marine terraces and the topmost rasa levels are shown in two tones of blue, with a lighter tone for more speculative surfaces (see main text). Bedding measurements are both from this study (TS) and the geological map (GM) of Danamos (1992). Observed onlap contacts between the largest uplited basin and basement are also shown. Insets show locations of Fig. 6 and Sup. Fig. 1. Green symbols mark the field photographs of Fig. 3 with viewing direction marked with arrows. Yellow stars mark the locations of samples dated by biostratigraphy (see results on Fig. 6); orange stars, near Mitata and W of Avlemonas, show location of Van Hinsbergen (2006) sites.*

3 Methods

3.1 Developing and analysing high-resolution DSMs derived from Pleiades imagery.

Tri-stereo Pleiades satellite images of 0.5 m resolution covering the whole island of Kythira were obtained through the ISIS and Tosca programs of the CNES. The open-source software MicMac (Rosu et al., 2015; Rupnik et al., 2016) was used to create tie-points, orientate the images and calculate 0.5 m-resolution DSMs, using ground control points at 0 m elevation for several locations along the coastline. To reduce the topographic effects of vegetation, crops and man-made structures, the DSMs were downsampled to 2 m resolution. Objects of ~50 cm height are easily detected, indicating a relative vertical accuracy of less than 1 m. The accuracy and refinement of our geologic/geomorphic map is relevantly improved thanks to usage of the Pleiades DSM in comparison to freely available digital elevation models (Supplementary Fig. 1). In addition, we also used stacked swaths of various sectors of the Pleiades DSM to gain a “2.5D” view of the topography. Stacked swaths (Armijo et al., 2015, Fernández-Blanco et al., 2019b) contain a significant number of parallel swath profiles derived from topographic data, which are plot together orthogonal to their strike as hairlines. By stacking swath profiles, the resulting profile highlights topographic coherence in depth (perpendicular to the viewpoint), allowing the distinction of structural and morphological features that are continuous over large scales. We share a georeferenced hillshade image and slope map of the 2 m-resolution Digital Surface Model through these links: https://doi.org/10.6084/m9.figshare.18715535.v1 (hillshade image) and https://doi.org/10.6084/m9.figshare.18714914.v1 (slope map). The map of Figure 2 can be downloaded in georeferenced format (as Geospatial PDF) at https://doi.org/10.6084/m9.figshare.18703496.v1.

3.2 Active faults and sedimentary basins

We carried out a detailed, albeit preliminary, mapping of faults, unit contacts and marine terraces and rasas by analyzing a combination of satellite imagery and DSM-derived hillshade maps, slope maps and topographic profiles. We carefully mapped contacts between the basement nappes and sedimentary basins as well as contacts within the basins, refining them from previous maps (Geological Map of Kythira Island – IGME, 1966; Danamos, 1992). During this stage prior to fieldwork, we also mapped the terraces semi-automatically, using the slope and roughness of the topography as guidelines, but evaluating every mapped terrace manually (section 3.4).

Fieldwork was carried out to verify and improve the mapped structures, study the terrace and fault morphologies in detail, resolve the stratigraphic contacts of Neogene deposits with the basement rocks, and understand the overall tectonic architecture of the sedimentary basins. All preliminary mapped faults were checked in the field to corroborate its correct mapping, and most faults presented a (sometimes degraded) fault scarp. We focused our analysis of the stratigraphic succession to the largest basin between Potamos and Avlemonas. Bedding measurements were taken at representative locations and kinematic indicators on fault scarps were measured using standard structural methods.

To quantify the overall strike of the active faults on Kythira, we subdivided them in 200-m segments, roughly corresponding to the smallest mapped faults, and placed them in bins of 5°. The same was done for all faults mapped on- and off-shore to the NE of the Hellenic Trench (Fig. 2) with 4-km long fault segments. Fault dip directions should be perpendicular to the strike of active faults. As a coarser but more objective alternative to measure the dominant fault strike offshore, we also quantified the slope direction of the bathymetry NE of the Hellenic Trench, calculating the 3x3 pixel slope direction for every ~200x200 m pixel. To a first order, the slope direction of steep slopes should be perpendicular to the strike of active faults.

3.3 Biostratigraphic dating

Marine foraminifer and ostracod species typically live(d) within a restricted water depth range, and within restricted time-intervals throughout geological history. As such, their occurrence in marine sediments - if not re-worked - can provide constraints on the age and/or paleodepth of those sediments. We sampled the deposits immediately below the uppermost marine sediments at 5 different sites for microfossil analysis (planktic and benthic foraminifers and ostracods), to obtain an approximate age for the formation of the rasa in locations around the area NE of Mitata (yellow stars on Fig. 2). These uppermost sediments typically form a 2-to-5 m-thick layer of coarse marine sandstones, rich in shells and oysters, acting as a caprock to the underlying finer sandstones that were sampled (Fig. 2).

Samples were soaked in a H_2O_2 5% solution for 24-48 hours, sieved under tap water using 0.066 and 0.125 mm mesh sieves, and dried in a 40°C oven. Whenever possible, up to 300 individuals were hand-picked from the dry sieved samples under a stereomicroscope, in order to collect a significant sample of the thanatocoenosis. The taxonomic identification of planktic foraminifers was based on Parker (1962), Postuma (1971), Kennett and Srinivasan (1983), Iaccarino et al. (2007), and Lirer et al. (2019). Benthic foraminifer classification was based on AGIP (1982), Morkhoven et al., (1986), and Meriç et al. (2014). For further visual comparison, we used the foraminifer databases of WoRMS, Foraminifera.eu, and www.microtax.org. The biostratigraphy of the study area was updated following the planktic foraminifer biozones of Lirer et al. (2019) and the Global Time Scale 2012 edited by Anthonissen and Ogg (2012). We took several pictures for identification under the Scanning Electron Microscope Philips XL30 (Suppl. Fig. 2).

3.4 Marine terrace analysis

Marine terraces are geomorphic markers that record the former position of the sea-level, and can thus be used to derive relevant information about vertical tectonic movements (e.g. Dupré, 1984; Armijo et al., 1996; De Gelder et al., 2019). The marine terraces on Kythira are wave-cut terraces, which are typically formed by wave-abrasion during sea-level rise and highstands (Anderson et al., 1999) and expressed as smooth planar surfaces with slope angles of 1°-15° (Scott and Pinter, 2003) that may be covered by a thin layer of sediments.

To map marine terraces, we used the surface classification model (SCM) of Bowles and Cowgill (2012) as a guideline to select surfaces with a low slope and roughness. After smoothing the DSM with a 6x6 m moving window, a roughness threshold of 3.5 was used to incorporate 90% of the data, and a slope threshold of 6° was used to avoid misinterpreting degraded paleo-cliffs, locally dipping as little as ~7°-9°. After removing the SCM surfaces that were clearly not terraces (e.g. man-made surfaces), high-confidence terraces were separated from more speculative terraces (strong and light blue polygons in Fig. 2). The speculative surfaces are those that either; 1) have a parallel orientation to the local bedding, typically in the Neogene sediments; 2) are not part of a staircase sequence; 3) are dipping slightly landwards rather than seawards; 4) have a geometry/location that could indicate they are river terraces; 5) might have been affected by agricultural structures; or 6) have a slope higher than the SCM threshold, but geometry, position, relative slope and imagery suggest that they are indeed marine terraces.

The shoreline angle of marine terraces, at the intersection of paleo-cliffs and paleo-platforms, approximates the sea level during former highstands (Lajoie, 1986; Merritts and Bull, 1989), but colluvial wedges caused by cliff degradation often obscure this angle (Hanks et al., 1984). For precise measurements of shoreline angles, we used TerraceM (Jara-Muñoz et al., 2016). Measurements were restricted to the eastern coast, where staircase sequences of terraces are least disturbed by cross-cutting faults and display a complete section between the coast and the upper rasa (Fig. 2). From field observations and DSM measurements, we estimated the slope of the present-day sea-cliff (Fig. 3) and used it as a proxy for the slope of eroded, older sea-cliffs. We obtained a range of possible shoreline angle elevations for every terrace in the selected area, by picking a most seaward/landward position of the paleo sea-cliff on the maximum elevations of cliff-perpendicular swath profiles and two points of the paleo-platform (Fig. 3; see De Gelder et al., 2015). We made a lateral correlation of terrace levels by comparing elevations of shoreline angles and their morphological characteristics (e.g., platform width, cliff height).

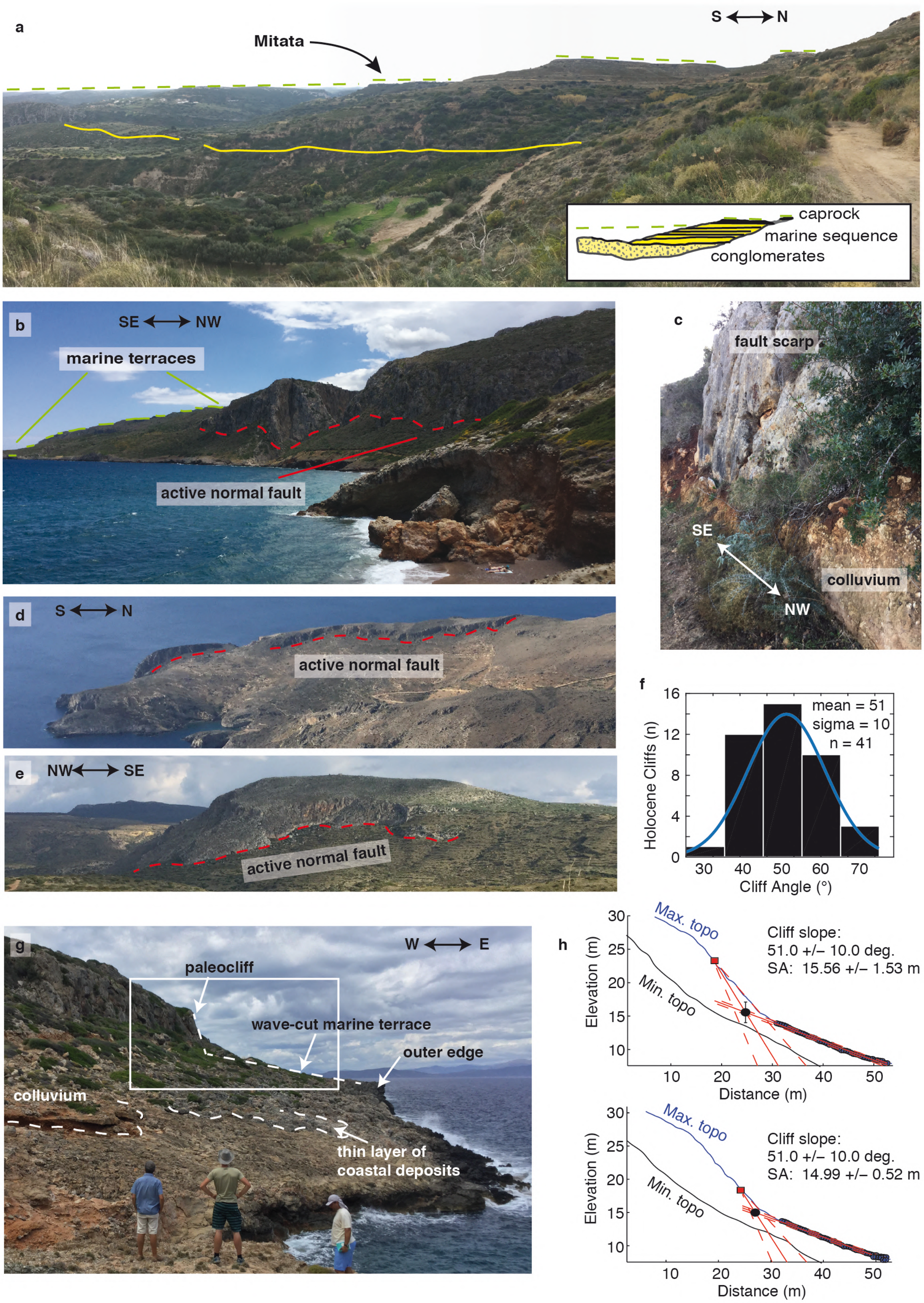
a
Mitata
S ⟷ N
caprock
marine sequence
conglomerates
b
SE ⟷ NW
marine terraces
active normal fault
c
fault scarp
SE
NW
colluvium
d
S ⟷ N
active normal fault
e
NW ⟷ SE
active normal fault
f
mean = 51
sigma = 10
n = 41
Holocene Cliffs (n)
Cliff Angle (°)
g
W ⟷ E
paleocliff
wave-cut marine terrace
outer edge
colluvium
thin layer of
coastal deposits
h
Max. topo
Min. topo
Cliff slope:
51.0 +/− 10.0 deg.
SA: 15.56 +/− 1.53 m
Elevation (m)
Distance (m)
Max. topo
Min. topo
Cliff slope:
51.0 +/− 10.0 deg.
SA: 14.99 +/− 0.52 m
Elevation (m)
Distance (m)

246

Figure 3*. *Field photographs and shoreline angle analysis. *Locations are given in Fig. 2.* ***(a)*** *Section of the basin stratigraphy taken E of Mitata; dashed line outlines the topmost rasa;* ***(b)*** *View of terraces and the fault south of Agia Pelagia along the NE-coast;* ***(c)*** *Detail of active fault scarp near Agia Pelagia;* ***(d)*** *Example of active N-S striking normal fault near Livadi;* ***(e)*** *Example of active NW-SE striking fault W of Avlemonas* ***(f)*** *Holocene cliff measurements along NE-coast;* ***(g)*** *Detail of marine terrace along the NE-coast near Plateia Ammos;* ***(h)*** *Example of shoreline angle analysis estimating a maximum (top) and minimum (bottom) position of the shoreline angle (SA).*

4 Results

4.1 Active faults

The geometry of most Neogene-Quaternary sedimentary basins is controlled by NW-SE trending normal faults. The largest basin, between Potamos and Avlemonas (Fig. 2; hereafter Potamos-Avlemonas Basin), is a half-graben bounded by faults along its SW margin (Fig. 4a), similar to the smaller basin near the coast east of Karvounades. The basins in the south of the island, bounding the SW coast and around Kalamos, Livadi and Kapsali, are partly onlapping on the basement, and partly bounded by NW-SE trending, and to a lesser extent N-S trending, normal faults. The basin in the north of the island, W of Plateia Ammos, is mostly onlapping on the basement, apart from its eastern margin, which is bounded by a N-S trending normal fault dipping to the west. N-S trending faults are also cross-cutting the Potamos-Avlemonas Basin, and the basement at several locations on the island. The area north of Potamos is largely devoid of fault scarps, which are probably unpreserved in the metamorphic rocks of the Arna Unit. Well-preserved fault scarps on both N-S and NW-SE trending faults indicate that both fault sets are active (examples in Fig. 3b-e). For the fault scarps that contained kinematic indicators, motion suggested nearly pure dip-slip motion along both sets of normal faults.

Taking the overall slope direction of the bathymetry, SW sloping directions towards the Hellenic Trench are the most common (Fig. 5a). When filtering out for higher slopes, which should be more representative of active faults, slope directions (dips) to the E and W are dominant (Figs. 5b, c), suggesting that ~N-S striking faults are more active. The separation of our mapped faults into distinct fault segments 200 m in length (Fig. 5d) indicates that N-S striking faults are most dominant on the island, especially E-dipping ones. NW-SE trending faults and trends in between N-S and NW-SE are less numerous, albeit only slightly. This result is very similar to the faults we mapped offshore in the SW Hellenic Arc (Fig. 5e), which trend N-S predominantly and NW-SE to a lesser extent.

These findings collectively indicate that extension is mostly E-W directed, and thus oblique to the trench direction, both on Kythira and on the scale of the SW Hellenic Arc. Trench-perpendicular NE-SW extension has played a dominant role in the formation of Neogene-Quaternary basins on Kythira bounded by NW-SE faults (Figs. 2, 5). It is still or again active, but is less important in accommodating active deformation. Trench-parallel NW-SE extension is minor or absent, both on the scale of Kythira and the scale of the SW Hellenic Arc.

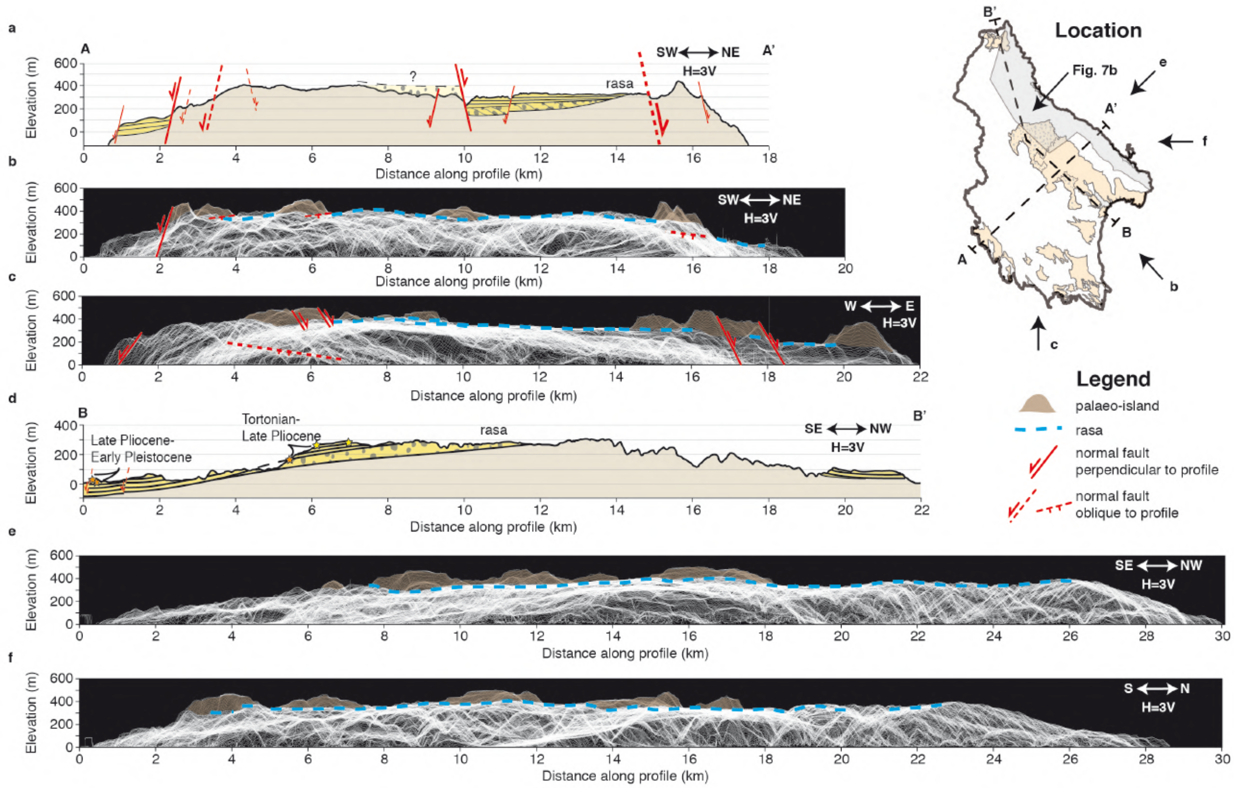

***Figure 4**. **Cross-sections and island-scale stacked swath profiles**. Top-right map shows locations of profiles in A-A' and B-B' on Kythira, as well as the viewing directions of the full-island stacked swaths in panels b, c, e and f, and the stacked swath location of Fig. 7b **(a)** NE-SW Cross-section perpendicular to major basin bounding faults. **(b)** Stacked swaths along a NE-SW strike. **(c)** Stacked swaths along an E-W strike. **(d)** NW-SE Cross-section along-strike of the*

major basin bounding faults. ***(e)*** *Stacked swaths along a NW-SE strike* ***(f)*** *stacked swaths along a N-S strike.*

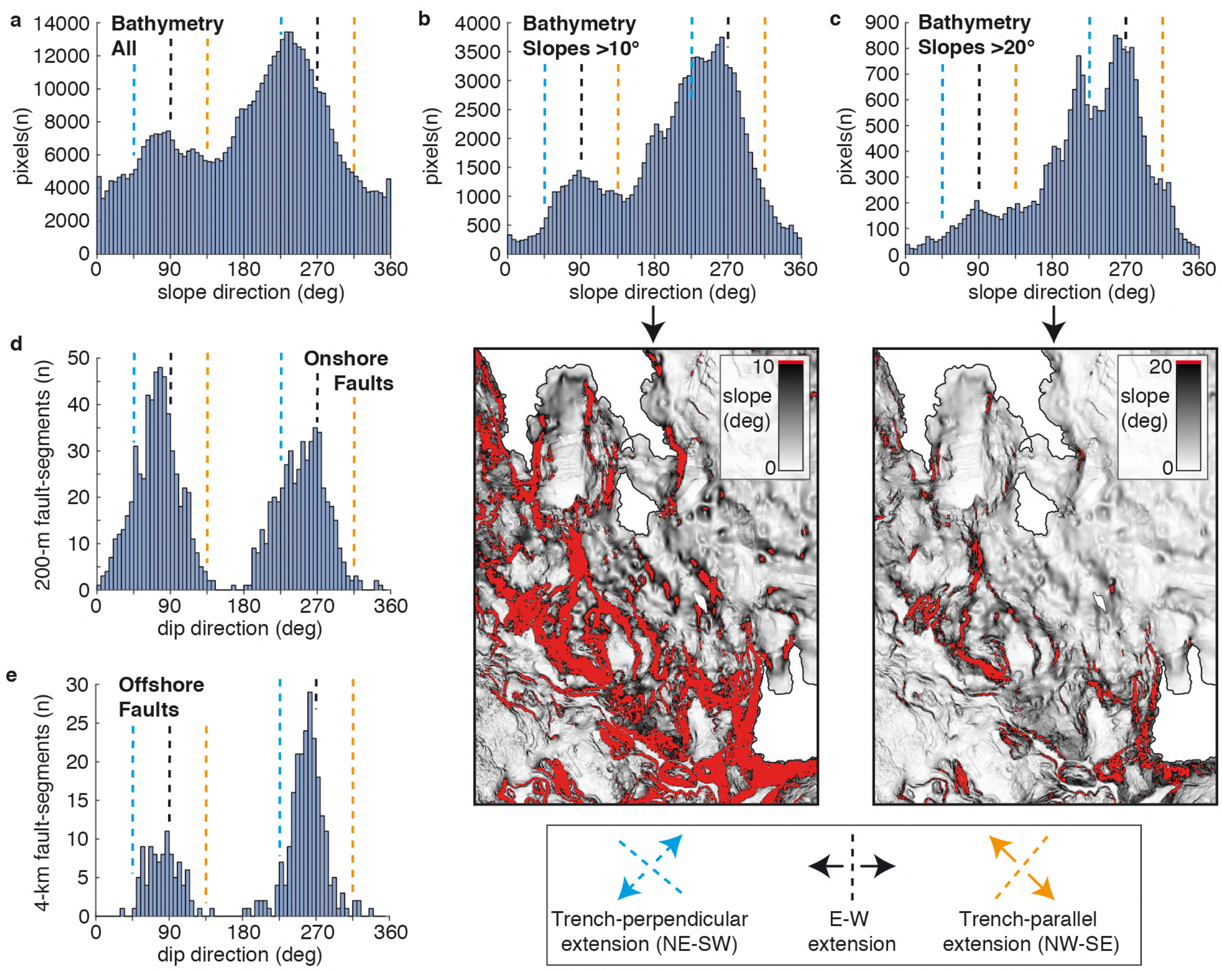

Figure 5*.* **Fault dip directions and slope directions.** ***(a)*** *Slope direction for all bathymetric data points NE of the Hellenic Trench in Fig. 2. To a first order, the slope direction of steep slopes should be perpendicular to the strike of active faults.* ***(b)*** *Same as* ***a****, but filtering data points that slope more than 10°, as plotted in map-view below.* ***(c)*** *Same as* ***b****, but for 20°.* ***(d)*** *Fault dip directions of 200-m fault segments mapped on Kythira in Fig. 2. Fault dip directions should be perpendicular to the strike of active normal faults* ***(e)*** *Fault dip directions of 4-km normal fault segments mapped within the bathymetry of the SW-Hellenic Arc of Fig. 1.*

4.2 Sedimentary basins

The stratigraphically lowest sedimentary infill in central Kythira consists of continental clastic deposits of variable grain size, including conglomerates, sandstones, siltstones and clays, and reaching a maximum thickness of ~100 m SE of Potamos (Figs. 2, 4a, d). The conglomerates that dominate the base of this section become gradually sparser up-section. These conglomerates are clast supported, and contain sub-rounded, polymict, and poorly sorted clasts of the three basement units, locally carving the basement with channel geometries. Imbrications and dip of infill deposits in those channels indicate transport towards the NE, similar to the present-day river reaching the coast near Agia Pelagia (Fig. 2). East of Mitata, the overlying marine deposits are deposited conformably on top of the continental deposits (Figs. 3a and 4a), in a gradual up-sequence transition from continental to coastal to shallow marine. Along the NE-margin of the Potamos-Avlemonas Basin, marine deposits are deposited directly on top of the basement (Fig. 4a). The marine deposits around Mitata and the rasa consist of limestones, sandstones and marls and are rich in *Pectinidae,* oysters and other macro-fossils, indicating a shallow marine environment. The marine deposits close to Avlemonas city consist mostly of laminated and homogeneous marls intercalated with coarse sandy limestone beds, and are poor in macro-fossils, possibly indicating a deeper marine environment.

The marine deposits are generally dipping ~0-10° to the SE (Fig. 4), and combined with the geometry of the continental-marine transition, indicate that the Potamos-Avlemonas basin is consistently 100-200 m thick, with larger content of continental deposits in its NW margin than towards its SE margin, where marine deposits dominate (Fig. 4d).

4.3 Micropaleontological analyses and biostratigraphy

Planktic and benthic foraminifers and ostracods were analyzed from five sites (Fig. 6a; Supplementary Table 1). Scanning electron microscope images of selected foraminifers and ostracods are presented in Supplementary Fig. 2. Ostracods were recovered in all the collected samples, while benthic foraminifers were absent in sample Qu. In general, they were well preserved and abundant, albeit not taxonomically diverse. Benthic foraminiferal assemblages consisted of a few reworked (Miocene) species, some eurybathic species and some other species typical of the infralittoral environment (approximately 0-50 m depth), such as *Elphidium* spp. (*E. advenum*, *E. complanatum*, *E. crispum*, *E. macellum*), *Asterigerinata planorbis*, *Aubignyana* *perlucida*, *Lobatula lobatula*, and *Cancris oblongus* (Morkhoven et al., 1986; Sgarella and Montcharmont Zei, 1993; Di Bella, 2010). Ostracod assemblages, mainly consisting of *Aurila* spp., *Callistocythere* spp., and *Semicytherura* spp., confirm a shallow infralittoral environment with vegetated bottom. Conversely, planktic foraminifers were collected only in sample Na, where several reworked species were identified together with some long-ranging (Miocene-Recent) species, and a few markers, such as *Globorotalia crassaformis*, *Globigerinoides extremus*, *Globigerinoides obliquus* and *Globigerinoides ruber*. On the base of their stratigraphic distribution (Lirer et al., 2019), the co-occurrence of these species in sample Na and the presence of the ostracod *Callistocythere parallela* in samples NA, Bc and Ta (Ruggieri and D'Arpa, 1993; D'Arpa and Ruggieri, 2004) constrain the age of the deposits immediately below the coastal rasa to the late Piacenzian-early Gelasian (2.8-2.4 Ma; Fig. 6b). Given its elevation of ~325 m above present sea level, this gives an average long-term uplift rate of ~0.13 mm/yr. This value is averaged over the last ~2.6 Ma, and should be taken as a minimum value.

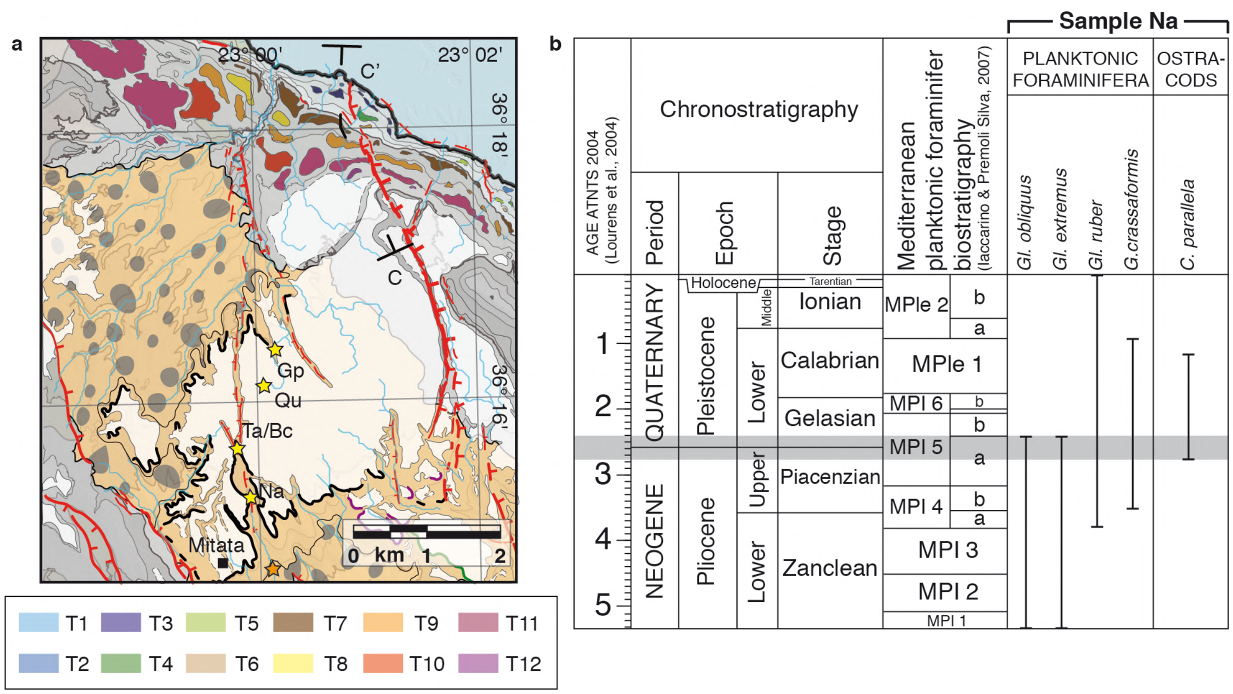

Figure 6*. Biostratigraphic dating results. (a)** *Zoom-in of Fig. 2 with location of samples used for biostratigraphic dating, as well as map of marine terraces for which shoreline angles were determined (Fig. 7a), and the location of profile C-C' (Fig. 8c)* ***(b) *Mediterranean planktic foraminifer biostratigraphic scheme of Pliocene-Quaternary, with the distribution of selected species of planktic foraminifers and ostracods recovered in sample Na. The grey band*

corresponds to the constrained age of the deposits immediately below the rasa. Timescale is after ATNTS 2004 (Lourens et al., 2004), and biostratigraphy after Lirer et al. (2019).

4.4 Marine terraces and rasa

The wide top-most rasa covers a large part of the island (Figs 2, 4), but is not preserved above the metamorphic Arna Unit in the northern part of the island. The very few topographic highs elevated above the rasa would have been paleo-islands when sea-level was around rasa elevations. These highs roughly follow the NW-SE trend of the basement nappes (Figs. 2, 4). As the rasa is only a few meters above the dated shallow marine deposits, it must be of younger age, ≤ 2.8-2.4 Ma (see above).

As for the rasa, the marine terraces are preserved within the Pindos and Tripolis basement units as well as in the sedimentary basins, but not within the metamorphic Arna Unit. Apart from the rasa caprock mentioned in section 3.3, similar caprocks of coastal deposits appear at the highest terrace levels within the Potamos-Avlemonas Basin (Fig. 2), in a low-angle unconformity with underlying marine basin deposits. Along the NE coast a thin layer of coastal deposits overlying the wave-cut platform exists at some locations (e.g. Fig. 3c), well cemented and containing sparse shell fragments. This layer typically dips seaward <5°, which is commonly much less than the bedding of the deformed basement.

Our detailed analysis of shoreline angles (Supplementary Fig. 4) reveals that the terraces along the NE coast are slightly tilted along the strike of the coastline over a distance of ~10 km (Fig. 7). The best-preserved and most continuous terraces are T7, T9 and T11 (Figs. 6b, 7), and decrease in elevation by ~25% over this distance. Other terraces are more scattered but can be correlated laterally following a similar trend. The continuity of marine terraces within the footwall of the Agia Pelagia Fault (Fig. 7a) indicates that it does not affect footwall uplift significantly. When looking at the scale of the whole island along four different projections the rasa is tilted eastward within the northwards view (Fig. 4c), varying from ~400 m elevation in the west to ~200 m in the east over a distance of ~15 km, and at a relatively constant ~400 m elevation in the westwards view (Fig. 4f). The trends in rasa elevation in the other viewing directions are more complicated (Figs. 4b, 4e). The above supports an overall island uplift with an approximately E-ward tilt. This is best compatible with a N-S striking source of uplift to the west of Kythira, which can also explain the along-coast tilt we see in the studied terraces (Fig. 7).

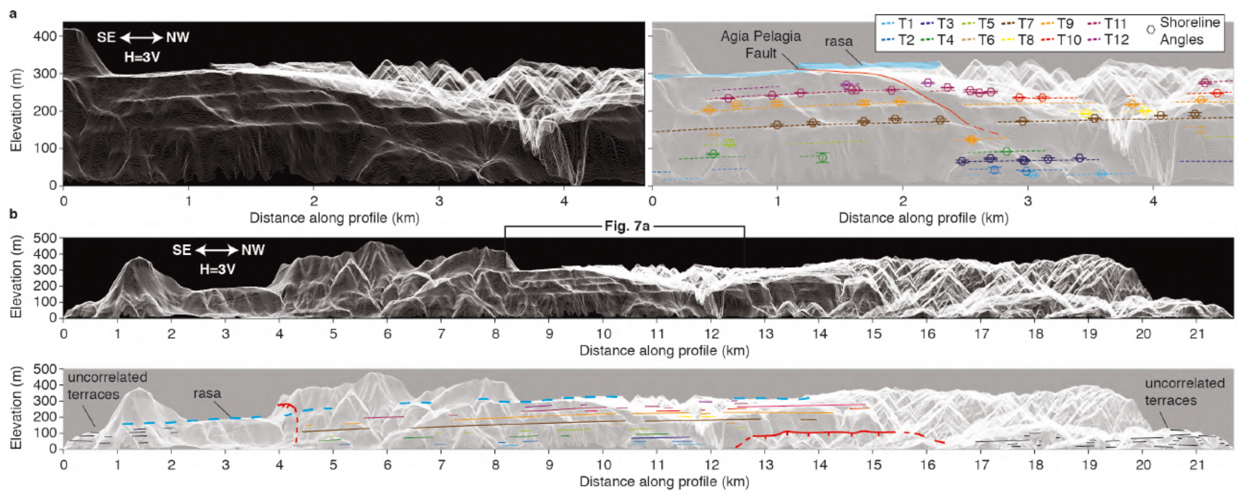

Figure 7**. **Terraces along the NE coast.** **(a)** Detail of stacked swath profile showing area for which shoreline angles were determined. Thin white lines represent 300 parallel swath profiles of 10 m width, with arrows indicating orientation of profiles. Shoreline angles and error bars of the twelve terrace levels (T1 to T12) are derived similarly to the example given in Fig. 3c, with details provided in Supplementary Fig. 4* ***(b) *Stacked swath profile of whole NE-coastline (top plot; location in Fig. 4), including trends of marine terraces and rasa (bottom plot).*

5 Discussion

5.1 Terrace correlation

Marine terraces are mainly formed during major interglacial sea-level highstands (e.g. Lajoie, 1986; Anderson et al., 1999). The most commonly recorded highstand within marine terrace sequences worldwide is the interglacial Marine Isotope Stage (MIS) 5e (Kopp et al., 2009, Pedoja et al., 2011; 2014). The MIS 5e peaked around 124±5 ka (e.g. Stirling et al., 1998; Masson-Delmotte et al., 2010) with eustatic sea-levels around 6±4 m higher than today (Murray-Wallace and Woodroffe, 2014). Given this, we expect one of the terraces of the sequence on Kythira to have been formed during MIS 5e. However, reliable ages of marine terraces on Kythira are lacking, making terrace attribution difficult. We thus estimate possible correlations of marine terraces to highstands based on the similar morphostratigraphy in the S-Peloponnese (Fig. 8).

Sequences of marine terraces on the Mani and Vatika peninsulas (Fig. 1) are also capped by wide Plio-Pleistocene rasas (e.g. Kelletat et al., 1976; Dufaure, 1977; Kleman et al., 2016) at comparable elevations (250-300 m asl) to the rasa in Kythira Island. The only radiometric dates in the region were taken at the Kalamakia cave on the Mani Peninsula (Fig. 8a). There, marine deposits ~2 m above present sea level are tentatively dated with U-Th as MIS 5c (~100 ka) (De Lumley et al., 1994). Assuming that this age is accurate, as well as constant uplift rates and a eustatic sea-level during MIS 5c of 5-40 m below present sea level (Fig. 8c; Spratt and Lisiecki, 2016), MIS 5e should be at an elevation of 8-54 m above present sea level. On the Vatika Peninsula, biostratigraphic evidence for Tyrrhenian deposits (~80-130 ka) is found on marine terraces at different elevations up to ~20 m above the present-day sea-level (Dufaure, 1970; Kelletat et al., 1976; Kowalczyk et al., 1992). The highest and oldest of those deposits (named Euthyrenian; Dufaure, 1970) would correspond to MIS 5e, now at ~20 m elevation in this peninsula. Assuming an uplift rate of the same order of magnitude for Kythira, we estimate the lowest terrace (T1, 31-35 m) or T2 (50-54 m) to correspond to MIS 5e. Taking into account MIS 5e elevation and age uncertainties mentioned above, this would imply uplift rates of ~0.22±0.04 mm/yr or ~0.37±0.04 mm/yr, or approximately 0.2-0.4 mm/yr. We extrapolated 0.22 and 0.37 mm/yr uplift rates to correlate marine terraces at higher elevations to older marine sea-level highstands up to 800 ka (Fig. 8c). If uplift rates have indeed been constant between the T1/T2 terraces and the highest well expressed marine terrace (T11), the latter would have an age of ~1.2-0.7 Ma. If uplift rates have been constant between the T1/T2 terraces and the rasa, the latter would have started emerging from the sea ~1.5-0.9 Ma.

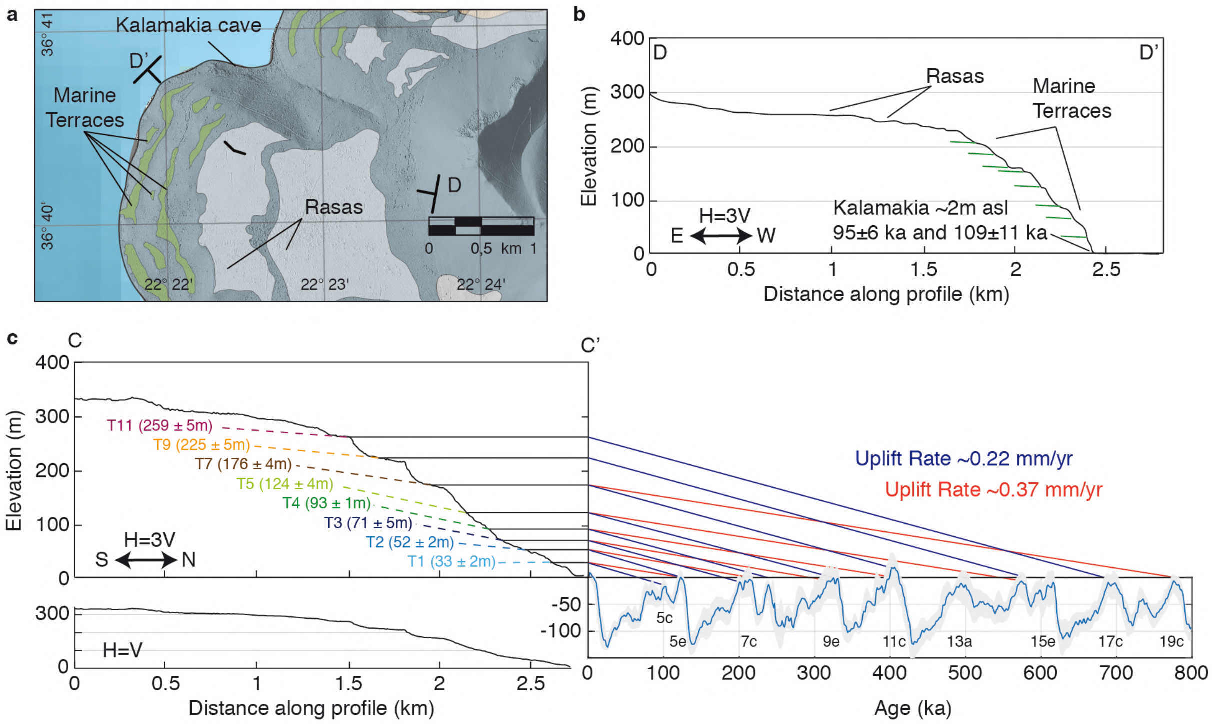

Figure 8. Proposed correlation of marine terraces to sea-level highstands. (a) *Map of terraces/rasas around the Kalamakia cave on the Mani Peninsula (location in Fig. 1)* ***(b)*** *Topographic profile D-D' of Kalamakia terrace sequence, derived from a Pleiades-DSM (as used for Kythira) with radiometric ages.* ***(c)*** *Correlation of main terrace levels to sea-level highstands, using the eustatic sea-level curve of Spratt and Lisiecki (2016) and the graphical method of Bloom and Yonekura (1990) adopting the shoreline angle elevations of profiles 31, 42 (T1), 18, 42 (T2), 15, 17, 19, 29, 30 (T3), 19 (T4), 16, 17 (T5), 14, 28 (T7), 10, 11 (T9), 11 and 22 (T11) (see Supplementary Fig. 4). The location of profile C-C' is specified in Fig. 6a.*

5.2 Uplift history

Whereas the age and elevation of the rasa indicate an uplift rate of ~0.12 mm/yr averaged over ~2.6 Ma for the center of the island (section 4.3), the Late Quaternary uplift rate estimates based on marine terraces are distinctly higher (0.2-0.4 mm/yr). Previous paleobathymetry estimates based on microfossils suggested another uplift history: initial rapid uplift of 2 mm/yr after ~2.3 Ma, followed by slower uplift of ~0.1 mm/yr since ~2 Ma (Van Hinsbergen et al., 2006). To discriminate between these potential scenarios of surface uplift, we used a simple landscape evolution model. We test 4 different scenarios (Fig. 9a): initial very rapid uplift (2 mm/yr) followed by slow uplift (0.1 mm/yr); constant slow uplift (0.12 mm/yr); initial slow uplift (0.05 mm/yr) followed by faster uplift (0.22 mm/yr); and stable conditions followed by rapid uplift (0.37 mm/yr). We use the cliff erosion model in TerraceM (Jara et al., 2019; adapted from Anderson et al., 1999), with standard parameter values for wave height (4 m), erosion rate (0.5 m/yr) and an initial slope based on the approximate slope of the sequence (12°). For simplicity, and to avoid biased results by sea-level noise inherent to long-term (>1 Ma) sea-level curves (De Gelder et al., 2020), we approximate Quaternary sea-level by combining a 40 ky-period, 65 m-amplitude sine function (2.6 - 1 Ma) and a 100 ky-period, 130-m amplitude sine function (Fig. 9b). Additional tests with different parameter values and published Plio-Quaternary sea-level curves are given in Supplementary Fig. 3, and do not change the main modeling outcomes.

The resulting first order morphology can be reproduced by the third and fourth scenarios. The first uplift scenario does not match the observed terrace sequence, as the decelerating uplift rate leads to the formation of a high cliff, since increased erosion due to re-occupation removes the older terraces. Slower uplift rates imply that terrace carving is distributed over a narrower vertical range, a process that was recently illustrated by Malatesta et al. (2021). The second scenario does not match the observed profile either. The change from ~40 ky period low-amplitude sea-level oscillations to ~100 ky period high-amplitude sea-level oscillations around the Mid-Pleistocene Transition (~1 Ma; Clark et al., 2006) should lead to a major change in morphology, which is not recorded by the marine terrace sequence in Kythira. In published Plio-Quaternary sea-level curves (Bintanja and V.d. Wal, 2008; De Boer et al., 2010; Bates et al., 2014 and Rohling et al., 2014) the change in sea-level oscillations is less abrupt, but also using those sea-level curves instead of the simplified one, big cliffs are at least twice as high as any cliff observed in the coastal morphology of Kythira (Supplementary Fig. 3). The third and the fourth scenarios are more compatible with the observed morphology of a continuous marine terrace sequence culminating in a wide rasa around 300 m elevation. Accounting for this, and for the ~0.22 and ~0.37 mm/yr uplift rates that are compatible with the marine terrace elevations, we favour an uplift history with initial stable conditions or slow uplift of Kythira from the sea, followed by faster uplift since ~1.5-0.7 Ma.

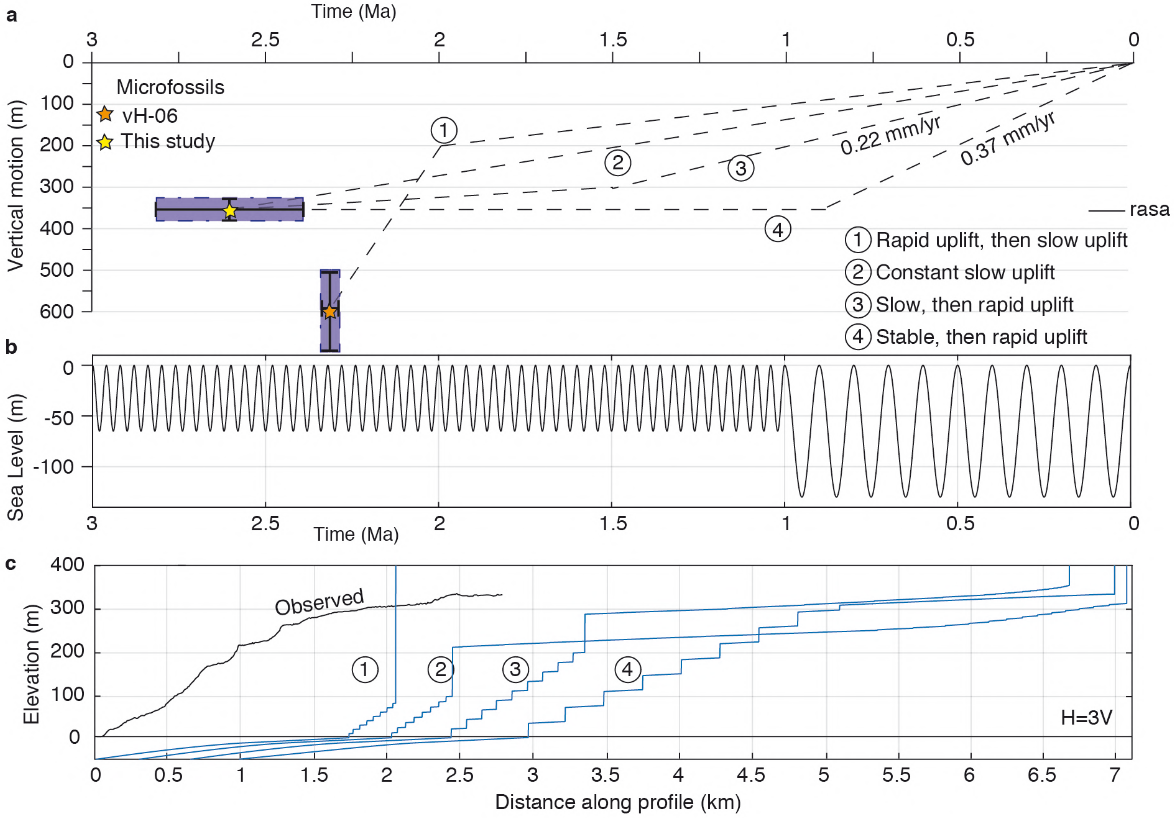

Figure 9. Landscape evolution modeling under different uplift scenarios. (a) *Different vertical motion scenarios, with scenario 1 assuming 400 m of rapid uplift followed by 200 m of slow uplift, as suggested by Van Hinsbergen et al. (2006), and scenarios 2, 3 and 4 assuming the dated samples of this study are equivalent to maximum transgression at ~2.6 Ma, and either steady slow uplift since then (scenario 2), a slow uplift followed by a rapid uplift (scenario 3 - uplift rate 0.22 mm/yr as estimated in Fig. 8) or stable conditions followed by a rapid uplift (scenario 4 - uplift rate 0.37 mm/yr as estimated in Fig. 8).* ***(b)*** *Extremely simplified sea-level curve used for the modeling (following De Gelder et al., 2020).* ***(c)*** *Modeling results for the different scenarios, compared to the terraced topography as given in Fig. 8. Parameter values are given in Supplementary Table 2.*

5.3 Miocene-Recent tectonics of Kythira Island

The sedimentary infill in the Potamos-Avlemonas Basin either infilled a former paleotopography after nappe stacking, or deposited in relation with the NW-SE striking normal faults that currently bound the basin. We favor the latter, fault-controlled sedimentation, on the basis of the lack of sedimentary deposits within the footwall of the basin-bounding normal faults (Fig. 4). This in turn supports that the ~100 m of relative subsidence between the Tortonian shallow marine deposits close to Mitata (Van Hinsbergen et al., 2006), and the shallow marine Plio-Pleistocene deposits dated in this study a few kms to the north (Figs. 2, 10), are largely of local origin and due to NE-SW extension. The geometry, depositional environment and ages of the sediments indicate that the coastline gradually shifted towards the NW with increasing subsidence, while the ~200 m thick basin transitioned laterally from continental conditions in the NW to marine conditions in the SE (Fig. 4). Within this framework, the Plio-Pleistocene section near Avlemonas (Fig. 2) (Van Hinsbergen et al., 2006) should have been deposited in a deeper marine environment than our dated deposits immediately below the rasa. Their vertical motion trend is very similar to ours, but when compared to our data, their paleo-depth estimate suggests much larger vertical motions (~400 m subsidence, ~800 m uplift). We did not find clear geologic or geomorphic evidence of marine conditions higher than the topmost rasa, and therefore suspect that the paleo-depth range of the fossils they considered is biased, possibly as a result of local upwelling. We did not observe the angular unconformity between continental and marine deposits described by Meulenkamp et al. (1977). As an explanation, we speculate that the Mediterranean sea-level drop of tens to hundreds of meters during the Messinian Salinity Crisis (MSC; 5.97-5.33 Ma) (Roveri et al., 2014) may have locally resulted in erosive/unconform sedimentary contacts near former river valleys, as described elsewhere in the Mediterranean (Bache et al., 2012).

We interpret the elevations and overall concave morphology of the terraces and overlying rasa as indicative of land motions at pace with sea-level variations or as a slow apparent uplift followed by faster uplift around ~1.5-0.7 Ma. The age of the rasa is coeval to that of the Mid-Pliocene Warm Period (~3.3-2.9 Ma; Rovere et al., 2014), after which eustatic sea-levels may have dropped by a few tens of meters (Raymo et al., 2011; Dutton et al., 2015). Therefore, an initial apparent uplift of Kythira could have been an effect of eustatic sea-level fall, and hence of climatic rather than tectonic origin. The rate and magnitude of the second uplift phase cannot be accounted for by eustatic sea-level changes alone, and implies a recent major change in tectonic conditions.

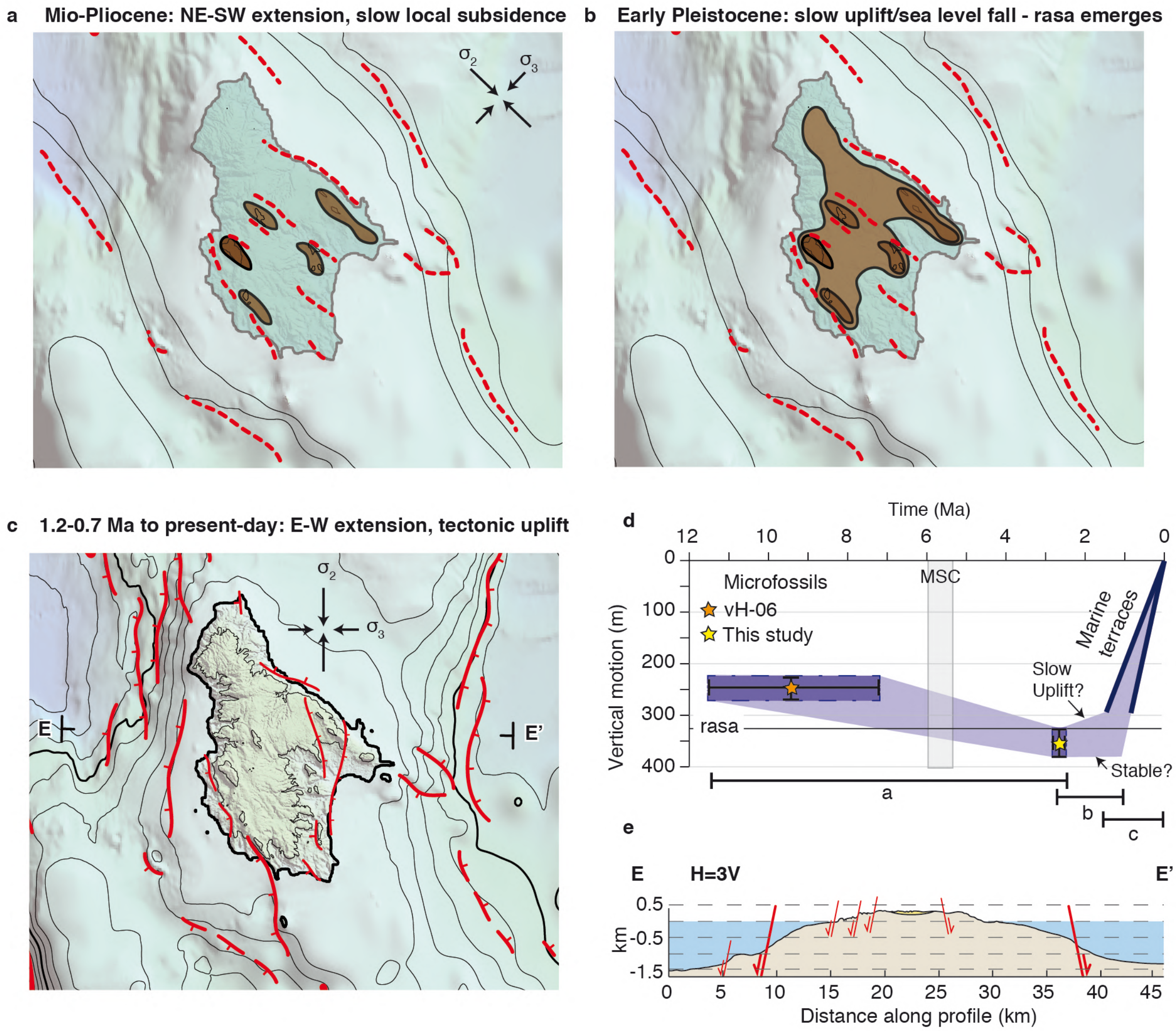

Figure 10. Schematic reconstruction of Miocene-Recent tectonic history of Kythira. (a) *Reconstruction for the phase of NE-SW extension during the Tortonian-Pliocene, resulting in NW-SE oriented topographic ridges and a large, coastal rasa in the latest Pliocene.* ***(b)*** *Reconstruction for the Early Pleistocene, with slow uplift resulting in emergence of the rasa from the sea* ***(c)*** *Reconstruction for the present-day setting, with dominantly E-W extension and uplift of the island as the results of offshore N-S trending normal faults.* ***(d)*** *Vertical motion, assuming a paleo-depth of our samples and the shallow marine Tortonian samples of Van Hinsbergen et al. (2006), of 0-50 m, and a marine terrace uplift rate of 0.22-0.37 mm/yr.*

5.4 Forearc uplift and regional implications

The N-S trending normal faults cutting through the topmost rasa and the Tortonian-Pliocene basin, and the associated surface uplift, post-date ~2.8-2.4 Ma. This supports that the uplift and overall eastward tilt of the rasa is due to the large N-S trending normal faults offshore (Fig. 10), and the uplift of Kythira as an asymmetric horst. These offshore faults would thus be of similar age as the N-S trending faults onshore but with larger vertical throws, >1 km (Fig. 10c). Given uplift to subsidence ratios of ~1:1-2.5 found for normal faults (King et al., 1988; McNeill et al., 2005, De Gelder et al., 2019), these N-S offshore faults can account for the ~200-400 m of observed uplift. Whereas we find an extreme lower bound for the onset of E-W extension and uplift of ~2.8-2.4 Ma, we deem it more likely that these events started as recently as ~1.5-0.7 Ma.

Our results on Kythira and in the offshore SW Hellenic Arc indicate that active extension is dominantly E-W oriented at a regional scale, at an oblique angle to the Hellenic Trench and the preceding phase of NE-SW extension. As shown in both analogue (Henza et al., 2011) and numerical models (e.g. Deng et al., 2018), preceding normal fault systems can be re-activated by a new phase of extension, even if that new phase has a different extension direction. The overall zigzag-pattern of the two active fault systems in the W Hellenic Forearc suggests that the NW-SE striking fault system was moderately well-developed (Henza et al., 2011) when the new phase of E-W extension initiated.

Several authors have interpreted the offshore faults in the SW Hellenic Arc as dominantly trench-normal and trench-perpendicular normal faults resulting from trench migration and slab-rollback (e.g. Angelier et al., 1982; van Hinsbergen and Schmidt, 2012; Gallen et al., 2014). E-W extension is difficult to reconcile with slab-rollback as a driving mechanism, and instead suggests that another mechanism must have induced the present-day deformation field. Sedimentary underplating has been highlighted by other studies as a potentially important driver of vertical motions around the Hellenic Forearc (Gallen et al., 2014; Menant et al., 2020). Although this can explain the cyclic pattern of Miocene-Pliocene subsidence followed by Pleistocene uplift on Kythira, there is no obvious explanation to link trench-perpendicular underplating with trench-oblique E-W extension. As such, we do not consider sedimentary underplating as a primary mechanism to explain tectonic changes in the SW Hellenic Arc.

A process that may explain Pleistocene changes around the forearc is the occurrence of slab tearing, which has been proposed for both the eastern (e.g. Özbakir et al., 2013) and western (e.g. Royden and Papanikolaou, 2011; Jolivet et al., 2013) limits of the Hellenic subduction zone. Given the location of Kythira, especially the W-limit of the Hellenic Arc is potentially relevant. Analogue models of slab-tearing, treating the Kefalonia Fault Zone (Fig. 11) as the strike-slip surface expression of the slab tear, suggest toroidal mantle flow would lead to ~NNE-SSW directed horizontal lithospheric strain in the Hellenic Forearc (Fig. 11; Guillaume et al., 2013). Although this does not perfectly match E-W extension, strain orientations are close enough that we cannot exclude the possibility that slab tearing plays a role in the SW Hellenic Arc deformation.

As proposed by Lyon-Caen et al. (1988) and Armijo et al. (1992), the change of extensional regime implies a change in boundary conditions, probably in relation to the nearby subduction zone. They suggested it could be due to incipient collision of the arc with the increasingly buoyant crust of the subducting African margin (Fig. 11). A similar tectonic-scale change in kinematics is supported by a wealth of evidence across the East Mediterranean (e.g., Mascle and Chaumillon, 1997; Schattner, 2010; Aksu et al., 2021), and in agreement with a growing body of observations. These include seismic and tomographic images, local bathymetric mapping and marine basins uplifted on land, all reporting changes in the stress and deformation fields throughout the Mediterranean in the last ~5 Ma (e.g., Prada et al., 2020; Zitellini et al., 2020; Gómez de la Peña et al., 2021).

A third possible process to explain tectonic changes in the forearc is the extrusion of the Anatolian plate towards the Aegean domain, controlled by the westward propagation of the North Anatolian Fault (NAF; Fig. 11; e.g. Armijo et al., 1996, 1999; Flerit et al, 2004). This process has been proposed as the cause of localized extension in the Corinth Rift (Fig. 11; e.g. Taymaz et al., 1991; Armijo et al., 1996; Taylor et al., 2011), which is currently extending at plate-boundary rates of 1-2 cm/yr (Briole et al., 2000). The initiation of localized rapid extension in the Corinth Rift around ~2-0.6 Ma (Armijo et al., 1996, Nixon et al., 2016, Gawthorpe et al., 2017, Fernández-Blanco et al., 2019a), is approximately coeval with the initiation of N-S fault-driven uplift we propose on Kythira, and we note that river profile inversion on Crete also suggests accelerated uplift over the past ~2 Ma (Roberts et al., 2013). The coeval timing of these events support that the recent growth into the Aegean of the propagating NAF changed the convergence rate on the Hellenic Trench, possibly doubling it within the Pleistocene (as proposed by Flerit et al. 2004). This could have resulted in stronger mechanical coupling on the deep subduction interface and an increase of the N-S directed horizontal forces, explaining the recent change in extensional fault geometry in the upper crust.

The three processes mentioned above, i.e. incipient collision, NAF propagation and slab tearing, can account for large-scale tectonic changes in the SW Hellenic Arc individually, but we emphasize that these processes are non-exclusive. As such, a combination of two or three of these processes, possibly inter-related, is also a feasible scenario.

In a more general sense, our study of Kythira Island highlights the importance of upper crustal faulting in forearc uplift. As mentioned above, the N-S striking offshore normal faults explain most, if not all of the observed uplift on Kythira. Deeper seated processes like underplating (e.g., Menant et al., 2020), dynamic topography (e.g., Conrad and Husson, 2009), lower-crustal mantle flow (e.g., Fernández-Blanco, 2014; Fernández-Blanco et al., 2020) and mantle flow in relation to roll-back and/or slab tearing (e.g., Guillaume et al., 2013) are likely to play a role in any subduction zone around the world, but their relative contributions are difficult to quantify if the forearc is crosscut with upper crustal faults. This is the case further east in the Hellenic Forearc (Gallen et al., 2014; Howell et al., 2017) as well as in many other subduction zones, like the Carribean (e.g. Leclerc et al., 2014), Japan (e.g. Matsu'ura et al., 2009) and New Zealand (e.g., Clark et al., 2010). A key factor to distinguish between uplift sources that we can underline from our study is the deformation pattern and wavelength. We know, from well-resolved examples like the Corinth Rift, that the deformation wavelength of upper crustal normal faults is around ~15-20 km (De Gelder et al., 2019). Whereas this is compatible with km-scale tilting on Kythira, the wavelength of lithospheric/mantle scale processes would be much larger, possibly by an order of magnitude. Continuous deformation markers such as marine terraces and rasas can be especially valuable in that sense, and are thus of primary importance in resolving uplift mechanisms at the front of overthrusting upper plates.

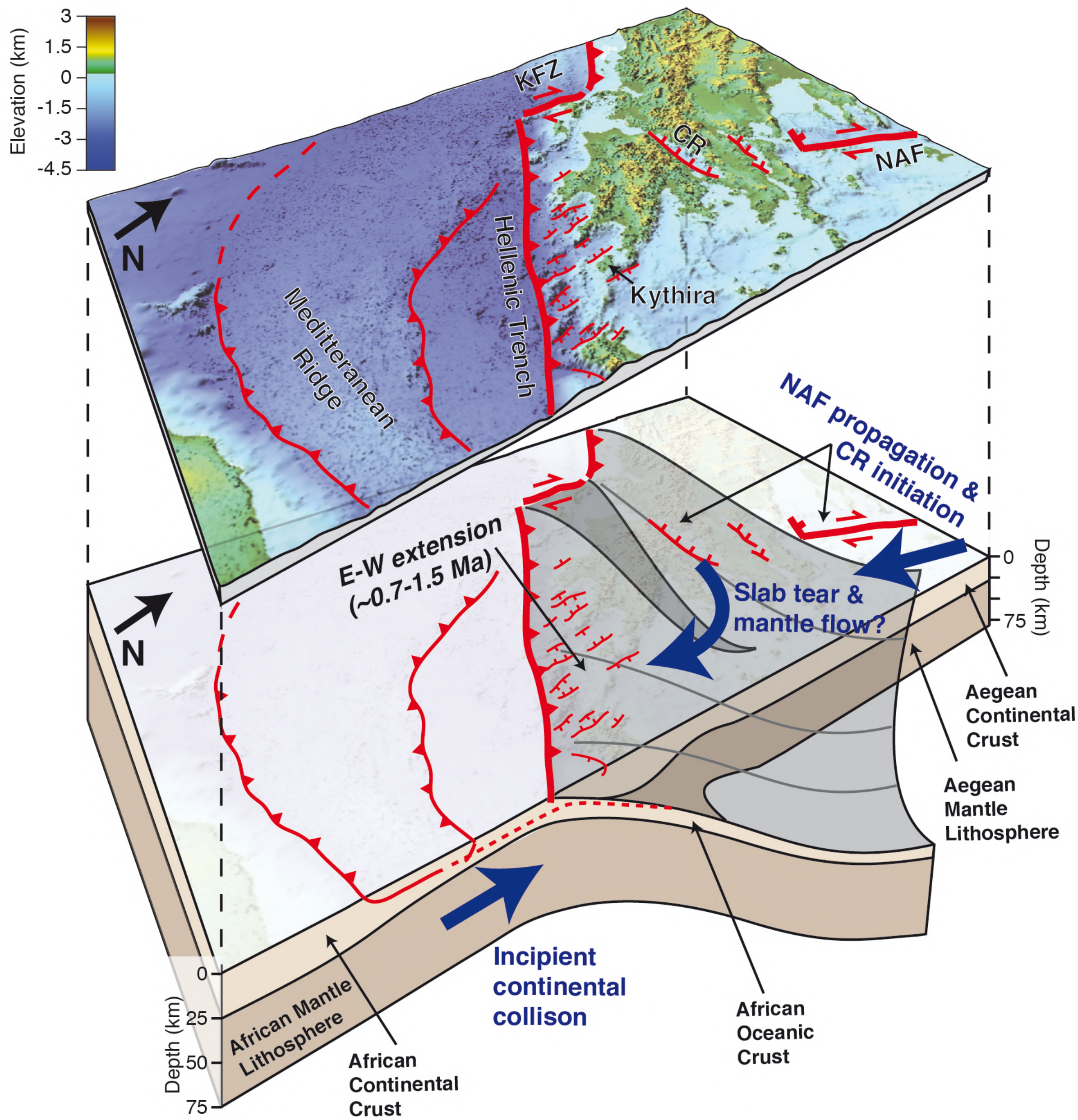

Figure 11. Possible regional drivers of E-W extension. *Top plot shows topo-bathymetry with main tectonic features, using a Global Mapper (version 15.0) 3D view and a 3x vertical exaggeration. Topography is an ALOS Global Digital Surface Model (DSM), and bathymetry is from the European Marine Observation and Data Network (EMODNet) Digital Terrain Model (DTM). KFZ = Kefalonia Fault Zone, CR = Corinth Rift and NAF = North Anatolian Fault. Bottom plot shows the same area but with underlying African and Aegean lithosphere. Marked in blue are 3 possible mechanisms, not mutually exclusive, that could have led to E-W extension*

since ~1.5-0.7 Ma. This plot is approximately to scale, with African lithospheric structure S of the Hellenic Trench based on Meier et al. (2004), Aegean lithospheric structure based on Jolivet et al. (2013) and schematic geometry of a possible slab tear based on Guillaume et al. (2013). There is some debate on the location of the main plate boundary (e.g. discussion in Shaw and Jackson, 2010), with estimates ranging from the Hellenic Trench to S of the Mediterranean Ridge, but this does not affect our main inferences.

6 Conclusions

Our study of the main tectono-stratigraphic and morphological features of Kythira allows us to draw the following conclusions:

1) Slow local subsidence of ~100 m within the largest sedimentary basin on Kythira occurred between the Tortonian and Latest Pliocene, possibly largely accommodated by a NW-SE trending fault system forming a half-graben.

2) The highest elevated marine deposits below a wide paleo-coastal rasa constrain maximum transgression to ~2.8-2.4 Ma, and give a maximum age for the onset of recent uplift.

3) Marine regression following rasa-formation occurred in two steps. The first phase occurs with stable conditions or slow uplift, possibly as an effect of eustatic sea-level drop instead of a tectonic origin. This phase was followed by a faster uplift phase of ~0.2-0.4 mm/yr that initiated around 1.5-0.7 Ma.

Our evidence supports that this last and ongoing phase of faster uplift is largely driven by N-S trending normal faults that are part of a regionally dominant mode of active E-W extension. We attribute the change in tectonic regime and vertical motion around 1.5-0.7 Ma to changing boundary conditions at the subduction zone in relation to incipient collision with the African plate, Aegean-Anatolian extrusion and propagation of the North Anatolian Fault, and/or slab tearing. In all those cases, increased N-S directed horizontal forces could have resulted in a new direction of extension and active uplift of horsts like Kythira. In general, we emphasize the importance of upper crustal faulting in dictating forearc uplift patterns.

Acknowledgments

The authors declare no conflicts of interest. The research leading to these results has received funding from the People Programme (Marie Curie Actions) of the European Union's Seventh Framework Programme under the ITN project ALErT (Grant FP7-PEOPLE-2013-ITN number 607996) and by the ISIS program of CNES. DF-B acknowledges as well the institutional support of the 'Severo Ochoa Centre of Excellence' accreditation (CEX2019-000928-S). The authors thank Arthur Delorme and Ewelina Rupnik for their technical assistance in producing the DSMs and Elsa Gliozzi and Domenico Cosentino for help with biostratigraphic dating. We thank the Interdepartmental Laboratory of Electron Microscopy (LIME) of Roma Tre University for the microfossil images. Numerical computations for the DSM were performed on the S-CAPAD platform, Institut de Physique du Globe de Paris (IPGP), France. This study contributes to the IdEx Université de Paris ANR-18-IDEX-0001. This is IPGP contribution no XXX

Availability Statement

The Pleiades satellite imagery was obtained through the ISIS and Tosca programs of the Centre National d'Etudes Spatiales (CNES, France) under an academic license and is not for open distribution. On request, we'll provide the DSM calculated from this imagery to any academic researcher who gets approval from CNES (contact isis-pleiades@cnes.fr for quoting this paper, and with lacassin@ipgp.fr in copy). We do share a georeferenced hillshade image and slope map of the 2 m-resolution Digital Surface Model that was developed from Pleiades satellite imagery. This image can be retrieved with these links:

https://doi.org/10.6084/m9.figshare.18715535.v1 (hillshade image)

https://doi.org/10.6084/m9.figshare.18714914.v1 (slope map).

The map of Figure 2 can be downloaded in georeferenced format (as Geospatial PDF) at https://doi.org/10.6084/m9.figshare.18703496.v1. The other data that support the findings of this study are available within the publication, referenced studies and/or from the corresponding author on request.

References

AGIP, 1982. Foraminiferi Padani (Terziario e Quaternario), 2nd ed. Milano.

Aksu, A. E., Hall, J., & Yaltırak, C. (2021). Miocene–Quaternary tectonic, kinematic and sedimentary evolution of the eastern Mediterranean Sea: A regional synthesis. Earth-Science Reviews, 220, 103719.

Anderson, R. S., Densmore, A. L., & Ellis, M. A. (1999). The generation and degradation of marine terraces. Basin Research, 11(1), 7–19.

Angelier, J., Lybéris, N., Le Pichon, X., Barrier, E., & Huchon, P. (1982). The tectonic development of the hellenic arc and the sea of crete: A synthesis. Tectonophysics, 86(1), 159–196.

Anthonissen, D.E., Ogg, J.G., 2012. Appendix 3. Cenozoic and Cretaceous Biochronology of Planktonic Foraminifera and Calcareous Nannofossils, in: Gradstein, F.M., Ogg, J.G., Schmitz, M.D., Ogg, G.M. (Eds.), The Geologic Time Scale 2012. Elsevier, Amsterdam, pp. 1083–1127.

Armijo, R., Lacassin, R., Coudurier-Curveur, A., & Carrizo, D. (2015). Coupled tectonic evolution of Andean orogeny and global climate. Earth-Science Reviews, 143, 1–35.

Armijo, R., Lyon-Caen, H., & Papanastassiou, D. (1992). East-west extension and Holocene normal-fault scarps in the Hellenic arc. Geology, 20(6), 491–494.

Armijo, R., Meyer, B., Hubert, A., & Barka, A. (1999). Westward propagation of the North Anatolian fault into the northern Aegean: Timing and kinematics. Geology, 27(3), 267–270.

Armijo, R., Meyer, B., King, G. C. P., Rigo, A., & Papanastassiou, D. (1996). Quaternary evolution of the Corinth Rift and its implications for the Late Cenozoic evolution of the Aegean. Geophysical Journal International, 126(1), 11–53.

Aubouin, J. (1957). Essai de correlations stratigraphiques en Grece occidentale. Bulletin de La Société Géologique de France, S6-VII(4-5), 281–304.

Bache, F., Popescu, S.-M., Rabineau, M., Gorini, C., Suc, J.-P., Clauzon, G., Olivet, J.-L., Rubino, J.-L., Melinte-Dobrinescu, M. C., Estrada, F., & Others. (2012). A two-step process for the reflooding of the Mediterranean after the Messinian Salinity Crisis. Basin Research, 24(2), 125–153.

Bates, S. L., Siddall, M., & Waelbroeck, C. (2014). Hydrographic variations in deep ocean temperature over the mid-Pleistocene transition. Quaternary Science Reviews, 88, 147–158.

Bintanja, R., & van de Wal, R. S. W. (2008). North American ice-sheet dynamics and the onset of 100,000-year glacial cycles. Nature, 454(7206), 869–872.

Bloom, A. L., & Yonekura, N. (1990). Graphic analysis of dislocated Quaternary shorelines. Sea-Level Change, 104–115.

Bowles, C. J., & Cowgill, E. (2012). Discovering marine terraces using airborne LiDAR along the Mendocino-Sonoma coast, northern California. Geosphere, 8(2), 386–402.

Briole, P., Rigo, A., Lyon-Caen, H., Ruegg, J. C., Papazissi, K., Mitsakaki, C., Balodimou, A., Veis, G., Hatzfeld, D., & Deschamps, A. (2000). Active deformation of the Corinth rift, Greece: Results from repeated Global Positioning System surveys between 1990 and 1995. Journal of Geophysical Research, 105(B11), 25605–25625.

Chabalier, J. B., Lyon-Caen, H., Zollo, A., Deschamps, A., Bernard, P., & Hatzfeld, D. (1992). A detailed analysis of microearthquakes in western Crete from digital three-component seismograms. Geophysical Journal International, 110(2), 347–360.

Clark, K., Berryman, K., Litchfield, N., Cochran, U., & Little, T. (2010). Evaluating the coastal deformation mechanisms of the Raukumara Peninsula, northern Hikurangi subduction margin, New Zealand and insights into forearc uplift processes. New Zealand Journal of Geology and Geophysics, 53(4), 341–358.

Clark, P. U., Archer, D., Pollard, D., Blum, J. D., Rial, J. A., Brovkin, V., Mix, A. C., Pisias, N. G., & Roy, M. (2006). The middle Pleistocene transition: characteristics, mechanisms, and implications for long-term changes in atmospheric pCO 2. Quaternary Science Reviews, 25(23), 3150–3184.

Conrad, C. P., & Husson, L. (2009). Influence of dynamic topography on sea level and its rate of change. Lithosphere. https://pubs.geoscienceworld.org/gsa/lithosphere/article-abstract/1/2/110/99489

Danamos, G. (1992). Contribution to the Geology and Hydrogeology of the island of Kythira. PhD thesis, Univesity of Athens, Athens.

D’arpa, C., & Ruggieri, G. (2004). Pliocene ostracofauna of the Altavilla section (Altavilla Milica, Sicily). Systematic Remarks. Bolletino de La Societa Paleontologica Italiana, 13, 159–180.

Davis, D., Suppe, J., & Dahlen, F. A. (1983). Mechanics of fold-and-thrust belts and accretionary wedges. Journal of Geophysical Research, [Solid Earth], 88(B2), 1153–1172.

Dawson, A. G., Dawson, S., Cooper, J. A. G., Gemmell, A., & Bates, R. (2013). A Pliocene age and origin for the strandflat of the Western Isles of Scotland: a speculative hypothesis. Geological Magazine, 150(2), 360–366.

de Boer, B., Van de Wal, R., Bintanja, R., Lourens, L. J., & Tuenter, E. (2010). Cenozoic global ice-volume and temperature simulations with 1-D ice-sheet models forced by benthic□ 18O records. Annals of Glaciology, 51(55), 23–33.

de Gelder, G., Fernández-Blanco, D., Lacassin, R., Armijo, R., Delorme, A., Jara-Muñoz, J., & Melnick, D. (2015). Corinth terraces re-visited: Improved paleoshoreline determination using Pleiades-DEMs. Geotectonic Research, 97, 12–14.

de Gelder, G., Fernández-Blanco, D., Melnick, D., Duclaux, G., Bell, R. E., Jara-Muñoz, J., Armijo, R., & Lacassin, R. (2019). Lithospheric flexure and rheology determined by climate cycle markers in the Corinth Rift. Scientific Reports, 9(1), 4260.

de Gelder, G., Jara-Muñoz, J., Melnick, D., Fernández-Blanco, D., Rouby, H., Pedoja, K., Husson, L., Armijo, R., & Lacassin, R. (2020). How do sea-level curves influence modeled marine terrace sequences? Quaternary Science Reviews, 229, 106132.

de Lumley, H., Darlas, A., Anglada, R., Cataliotti-Valdina, J., Desclaux, E., Dubar, M., Falguères, C., Keraudren, B., Lecervoisier, B., Mestour, B., & Others. (1994). Grotte de Kalamakia (Aéropolis, Péloponnèse). Bulletin de Correspondance Hellénique, 118(2), 535–559.

Deng, C., Gawthorpe, R. L., Fossen, H., & Finch, E. (2018). How does the orientation of a preexisting basement weakness influence fault development during renewed rifting? Insights from three-dimensional discrete element modeling. Tectonics, 37(7), 2221–2242.

Di Bella, L., 2010. Plio-Pleistocene foraminiferal assemblages of the Monte Mario site (Rome, Italy). Boll. Della Soc. Paleontol. Ital. 49, 145–161.

Dufaure, J.-J. (1970). Niveaux d’abrasion marine quaternaires autour du Péloponèse. Annales de Géographie, 79(433), 325–342.

Dufaure, J.-J. (1977). Néotectonique et morphogenèse dans une péninsule méditerranéenne: Le Péloponnèse. Revue de Géographie Physique et de Géologie Dynamique, 19, 27–58.

Dupré, W. R. (1984). Reconstruction of paleo-wave conditions during the Late Pleistocene from marine terrace deposits, Monterey Bay, California. Marine Geology, 60(1), 435–454.

Dutton, A., Carlson, A. E., Long, A. J., Milne, G. A., Clark, P. U., DeConto, R., Horton, B. P., Rahmstorf, S., & Raymo, M. E. (2015). Sea-level rise due to polar ice-sheet mass loss during past warm periods. Science, 349(6244), aaa4019.

Ekström, G., Nettles, M., & Dziewoński, A. M. (2012). The global CMT project 2004–2010: Centroid-moment tensors for 13,017 earthquakes. Physics of the Earth and Planetary Interiors, 200-201, 1–9.

England, P., Houseman, G., & Nocquet, J.-M. (2016). Constraints from GPS measurements on the dynamics of deformation in Anatolia and the Aegean. Journal of Geophysical Research, [Solid Earth], 121(12), 8888–8916.

Faccenna, C., Jolivet, L., Piromallo, C., & Morelli, A. (2003). Subduction and the depth of convection in the Mediterranean mantle. Journal of Geophysical Research, 108(B2), 2099.

Fernández-Blanco, D. (2014). Evolution of Orogenic Plateaus at Subduction Zones - Sinking and raising the southern margin of the Central Anatolian Plateau. https://doi.org/10.31237/osf.io/hf759

Fernández-Blanco, D., de Gelder, G., Lacassin, R., & Armijo, R. (2019a). A new crustal fault formed the modern Corinth Rift. Earth Science Reviews, 199(102919).

Fernández-Blanco, D., Gelder, G., Lacassin, R., & Armijo, R. (2019b). Geometry of flexural uplift by continental rifting in Corinth, Greece. Tectonics. https://doi.org/10.1029/2019TC005685

Fernández-Blanco, D., Mannu, U., Bertotti, G., & Willett, S. D. (2020). Forearc high uplift by lower crustal flow during growth of the Cyprus-Anatolian margin. Earth and Planetary Science Letters, 544, 116314.

Flerit, F., Armijo, R., King, G., & Meyer, B. (2004). The mechanical interaction between the propagating North Anatolian Fault and the back-arc extension in the Aegean. Earth and Planetary Science Letters, 224(3), 347–362.

Fuller, C. W., Willett, S. D., & Brandon, M. T. (2006). Formation of forearc basins and their influence on subduction zone earthquakes. Geology, 34(2), 65–68.

Gaki-Papanastassiou, K., Maroukian, H., & Kourmpanian, V. (2011). The morphotectonic evolution of southern half of Kythira Island (Ionian sea, Greece) during the Quaternary. Prace Geograficzne, 0(127). http://www.ejournals.eu/sj/index.php/PG/article/view/4208

Gallen, S. F., Wegmann, K. W., Bohnenstiehl, D. R., Pazzaglia, F. J., Brandon, M. T., & Fassoulas, C. (2014). Active simultaneous uplift and margin-normal extension in a forearc high, Crete, Greece. Earth and Planetary Science Letters, 398, 11–24.

Gawthorpe, R., Leeder, M., Kranis, H., Skourtsos, E., Andrews, J., Henstra, G., Mack, G., Muravchik, M., Turner, J., & Stamatakis, M. (2017). Tectono-sedimentary evolution of the Plio-Pleistocene Corinth rift, Greece. Basin Research. http://onlinelibrary.wiley.com/doi/10.1111/bre.12260/full

Gerolymatos, I. K. (1994). Metamorphose und Tektonik der Phyllit-Quarzit-Serie und der Tyros-Schichten auf dem Peloponnes und Kythira (Vol. 164). Selbstv. Fachbereich Geowissenschaften, FUB.

Gómez de la Peña, L., R. Ranero, C., Gràcia, E., & Booth-Rea, G. (2021). The evolution of the westernmost Mediterranean basins. Earth-Science Reviews, 214, 103445.

Guilcher, A. (1974). Les rasas: un problème de morphologie littorale générale. Annales de Géographie, 1–33.

Guillaume, B., Husson, L., Funiciello, F., & Faccenna, C. (2013). The dynamics of laterally variable subductions: laboratory models applied to the Hellenides. Solid Earth, 4(2), 179.

Gutscher, M.-A., Kukowski, N., Malavieille, J., & Lallemand, S. (1996). Cyclical behavior of thrust wedges: Insights from high basal friction sandbox experiments. Geology, 24(2), 135–138.

Hanks, T. C., Bucknam, R. C., Lajoie, K. R., & Wallace, R. E. (1984). Modification of wave-cut and faulting-controlled landforms. Journal of Geophysical Research, [Solid Earth], 89(B7), 5771–5790.

Henza, A. A., Withjack, M. O., & Schlische, R. W. (2011). How do the properties of a pre-existing normal-fault population influence fault development during a subsequent phase of extension? Journal of Structural Geology, 33(9), 1312–1324.

Howell, A., Jackson, J., Copley, A., McKenzie, D., & Nissen, E. (2017). Subduction and vertical coastal motions in the eastern Mediterranean. Geophysical Journal International, 211(1), 593–620.

Iaccarino, S. M., Premoli Silva, I., Biolzi, M., Foresi, L. M., Lirer, F., Turco, E., & Petrizzo, M. R. (2007). Practical manual of Neogene planktonic foraminifera. https://air.unimi.it/handle/2434/41563

Institute of Geology and Mining Research (IGME), 1966, Geological map of Kythira island 1:50.000.

Jacobshagen, V. (1987). Geologie von Griechenland. http://www.schweizerbart.de/publications/detail/isbn/9783443110192/%23

Jara-Muñoz, J., Melnick, D., Brill, D., & Strecker, M. R. (2015). Segmentation of the 2010 Maule Chile earthquake rupture from a joint analysis of uplifted marine terraces and seismic-cycle deformation patterns. Quaternary Science Reviews, 113, 171–192.

Jara-Muñoz, J., Melnick, D., Pedoja, K., & Strecker, M. R. (2019). TerraceM-2: A Matlab® interface for mapping and modelling marine and lacustrine terraces. Frontiers of Earth Science in China, 7, 255.

Jara-Muñoz, J., Melnick, D., & Strecker, M. R. (2016). TerraceM: A MATLAB® tool to analyze marine and lacustrine terraces using high-resolution topography. Geosphere, 12(1), 176–195.

Jolivet, L., & Brun, J.-P. (2010). Cenozoic geodynamic evolution of the Aegean. International Journal of Earth Sciences, 99(1), 109–138.

Jolivet, L., Faccenna, C., Huet, B., Labrousse, L., Le Pourhiet, L., Lacombe, O., Lecomte, E., Burov, E., Denèle, Y., Brun, J.-P., Philippon, M., Paul, A., Salaün, G., Karabulut, H., Piromallo, C., Monié, P., Gueydan, F., Okay, A. I., Oberhänsli, R., … Driussi, O. (2013). Aegean tectonics: Strain localisation, slab tearing and trench retreat. Tectonophysics, 597, 1–33.

Kelletat, D., Kowalczyk, G., Schröder, B., & Winter, K.-P. (1976). A synoptic view on the neotectonic development of the Peloponnesian coastal regions. Zeitschrift Der Deutschen Geologischen Gesellschaft, 447–465.

Kennett, J.P., Srinivasan, S.M., 1983. Neogene Planktonic Foraminifera: A Phylogenetic Atlas. Hutchinson Ross Publishing Company, Pennsylvania.

King, G. C. P., Stein, R. S., & Rundle, J. (1988). The growth of geological structures by repeated earthquakes, 2: Field examples of continental dip-slip faults. Journal of Geophysical Research, 93, 13319–13331.

Kleman, J., Borgström, I., Skelton, A., & Hall, A. (2016). Landscape evolution and landform inheritance in tectonically active regions: The case of the Southwestern Peloponnese, Greece. Zeitschrift F??r Geomorphologie, 60(2), 171–193.

Konstantinou, K. I., Kalogeras, I. S., Melis, N. S., Kourouzidis, M. C., & Stavrakakis, G. N. (2006). The 8 January 2006 earthquake (M w 6.7) offshore Kythira Island, southern Greece: seismological, strong-motion, and macroseismic observations of an intermediate-depth event. Seismological Research Letters, 77(5), 544–553.

Kopp, R. E., Simons, F. J., Mitrovica, J. X., Maloof, A. C., & Oppenheimer, M. (2009). Probabilistic assessment of sea level during the last interglacial stage. Nature, 462(7275), 863–867.

Kowalczyk, G., Reisch, L., Steinich, G., & Winter, K.-P. (1992). Jungpleistozaene Strandterrassen in Suedost-Lakonien (Peloponnes, Griechenland). Verlag der Gesellschaft für Geologische Wissenschaften.

Lajoie, K. R. (1986). Coastal tectonics. Active Tectonics.

Larroque, C., Calassou, S., Malavieille, J., & Chanier, F. (1995). Experimental modelling of forearc basin development during accretionary wedge growth. Basin Research, 7(3), 255–268.

Leclerc, F., Feuillet, N., Cabioch, G., Deplus, C., Lebrun, J. F., Bazin, S., Beauducel, F., Boudon, G., LeFriant, A., De Min, L., & Melezan, D. (2014). The Holocene drowned reef of Les Saintes plateau as witness of a long-term tectonic subsidence along the Lesser Antilles volcanic arc in Guadeloupe. Marine Geology, 355, 115–135.

Lirer, F., Foresi, L.M., Iaccarino, S.M., Salvatorini, G., Turco, E., Cosentino, C., Sierro, F.J., Caruso, A., 2019. Mediterranean Neogene planktonic foraminifer biozonation and biochronology. Earth-Science Rev. 196, 102869. https://doi.org/10.1016/j.earscirev.2019.05.013

Lourens, L. J., Hilgen, F. J., Laskar, J., Shackleton, N. J., & Wilson, D. (2004). A geological time scale 2004.

Lyberis, N., Angelier, J., Barrier, E., & Lallemant, S. (1982). Active deformation of a segment of arc: the strait of Kythira, Hellenic arc, Greece. Journal of Structural Geology, 4(3), 299–311.

Lyon-Caen, H. et al, Armijo, R., Drakopoulos, J., Baskoutass, J., Delibassis, N., Gaulon, R., Kouskouna, V., Latoussakis, J., Makropoulos, K., Papadimitriou, P., & Others. (1988). The 1986 Kalamata (South Peloponnesus) earthquake: Detailed study of a normal fault, evidences for east-west extension in the Hellenic Arc. Journal of Geophysical Research, [Solid Earth], 93(B12), 14967–15000.

Malatesta, L. C., Finnegan, N. J., Huppert, K. L., & Carreño, E. I. (2021). The influence of rock uplift rate on the formation and preservation of individual marine terraces during multiple sea-level stands. Geology. https://doi.org/10.1130/G49245.1

Manolessos, N. (1955). A further aid for the knowledge of the geology of the island Kythira. Annales Géologiques Des Pays Helléniques, 6, 51–80.

Marsellos, A. E., & Kidd, W. S. F. (2008). Extension and Exhumation of the Hellenic Forearc Ridge in Kythera. The Journal of Geology, 116(6), 640–651.

Marsellos, A. E., Min, K., & Foster, D. A. (2014). Rapid Exhumation of High-Pressure Metamorphic Rocks in Kythera-Peloponnese (Greece) Revealed by Apatite (U-Th)/He Thermochronology. The Journal of Geology, 122(4), 381–396.

Mascle, J., & Chaumillon, E. (1997). Pre-collisional geodynamics of the Mediterranean Sea: the Mediterranean Ridge and the Tyrrhenian Sea. https://www.earth-prints.org/handle/2122/1511

Masson-Delmotte, V., Stenni, B., Pol, K., Braconnot, P., Cattani, O., Falourd, S., Kageyama, M., Jouzel, J., Landais, A., Minster, B., Barnola, J. M., Chappellaz, J., Krinner, G., Johnsen, S., Röthlisberger, R., Hansen, J., Mikolajewicz, U., & Otto-Bliesner, B. (2010). EPICA Dome C record of glacial and interglacial intensities. Quaternary Science Reviews, 29(1–2), 113–128.

Matsu'ura, T., Furusawa, A., & Saomoto, H. (2009). Long-term and short-term vertical velocity profiles across the forearc in the NE Japan subduction zone. Quaternary Research, 71(2), 227–238.

McClusky, S., Balassanian, S., Barka, A., Demir, C., Ergintav, S., Georgiev, I., Gurkan, O., Hamburger, M., Hurst, K., Kahle, H., Kastens, K., Kekelidze, G., King, R., Kotzev, V., Lenk, O., Mahmoud, S., Mishin, A., Nadariya, M., Ouzounis, A., … Veis, G. (2000). Global Positioning System constraints on plate kinematics and dynamics in the eastern Mediterranean and Caucasus. Journal of Geophysical Research, 105(B3), 5695–5719.

McNeill, L. C., Collier, R. E. L., De Martini, P. M., Pantosti, D., & D'Addezio, G. (2005). Recent history of the Eastern Eliki Fault, Gulf of Corinth: geomorphology, palaeoseismology and impact on palaeoenvironments. Geophysical Journal International, 161(1), 154–166.

Meier, T., Rische, M., Endrun, B., Vafidis, A., & Harjes, H. P. (2004). Seismicity of the Hellenic subduction zone in the area of western and central Crete observed by temporary local seismic networks. Tectonophysics, 383(3-4), 149-169.

Menant, A., Angiboust, S., Gerya, T., Lacassin, R., Simoes, M., & Grandin, R. (2020). Transient stripping of subducting slabs controls periodic forearc uplift. Nature Communications, 11(1), 1823.

Meriç, E., Avşar, N., Yokeş, M.B., Dinçer, F., 2014. Atlas of recent benthic foraminifera from Turkey. Micropaleontology 60, 211–398.

Merritts, D., & Bull, W. B. (1989). Interpreting Quaternary uplift rates at the Mendocino triple junction, northern California, from uplifted marine terraces. Geology, 17(11), 1020–1024.

Meulenkamp, J. E., Theodoropoulos, P., & Tsapralis, V. (1977). Remarks on the Neogene of Kythira, Greece. Proceedings of the VI Colloqium on the Geology of the Aegean Region, 1, 355–362.

Morkhoven, F., Berggren, W., Edwards, A., 1986. Cenozoic Cosmopolitan Deep-water Benthic Foraminifera. Bull. Centres Rech. Explor.-Prod. Elf-Aquitaine, Mem, Pau.

Murray-Wallace, C. V., & Woodroffe, C. D. (2014). Quaternary Sea-Level Changes: A Global Perspective. Cambridge University Press.

Nixon, C. W., McNeill, L. C., Bull, J. M., Bell, R. E., Gawthorpe, R. L., Henstock, T. J., Christodoulou, D., Ford, M., Taylor, B., Sakellariou, D., Ferentinos, G., Papatheodorou, G., Leeder, M. R., Collier, R. E. L. I., Goodliffe, A. M., Sachpazi, M., & Kranis, H. (2016). Rapid spatiotemporal variations in rift structure during development of the Corinth Rift, central Greece. Tectonics, 35(5), 2015TC004026.

Özbakır, A. D., Şengör, A. M. C., Wortel, M. J. R., & Govers, R. (2013). The Pliny–Strabo trench region: A large shear zone resulting from slab tearing. Earth and Planetary Science Letters, 375, 188–195.

Papadopoulos, G. A., & Vassilopoulou, A. (2001). Historical and Archaeological Evidence of Earthquakes and Tsunamis Felt in the Kythira Strait, Greece. In Tsunami Research at the End of a Critical Decade (pp. 119–138). Springer, Dordrecht.

Papanikolaou, D., & Danamos, G. (1991). The role of the geotectonic location of Kythira and Cyclades in the geodynamic evolution of the Hellenic Arc. Bulletin of the Geological Society of Greece, 25(1), 65–79.

Parker, F.L., 1962. Planktonic foraminiferal species in Pacific sediments. Micropalentology 8, 219–254.

Pedoja, K., Husson, L., Johnson, M. E., Melnick, D., Witt, C., Pochat, S., Nexer, M., Delcaillau, B., Pinegina, T., Poprawski, Y., Authemayou, C., Elliot, M., Regard, V., & Garestier, F. (2014). Coastal staircase sequences reflecting sea-level oscillations and tectonic uplift during the Quaternary and Neogene. Earth-Science Reviews, 132, 13–38.

Pedoja, K., Husson, L., Regard, V., Cobbold, P. R., Ostanciaux, E., Johnson, M. E., Kershaw, S., Saillard, M., Martinod, J., Furgerot, L., Weill, P., & Delcaillau, B. (2011). Relative sea-level fall since the last interglacial stage: Are coasts uplifting worldwide? Earth-Science Reviews, 108(1), 1–15.

Pedoja, K., Ortlieb, L., Dumont, J. F., Lamothe, M., Ghaleb, B., Auclair, M., & Labrousse, B. (2006). Quaternary coastal uplift along the Talara Arc (Ecuador, Northern Peru) from new marine terrace data. Marine Geology, 228(1), 73–91.

Prada, M., Ranero, C. R., Sallares, V., Grevemeyer, I., de Franco, R., Gervasi, A., & Zitellini, N. (2020). The structure of Mediterranean arcs: New insights from the Calabrian Arc subduction system. Earth and Planetary Science Letters, 548, 116480.

Raymo, M. E., Mitrovica, J. X., O'Leary, M. J., DeConto, R. M., & Hearty, P. J. (2011). Departures from eustasy in Pliocene sea-level records. Nature Geoscience, 4(5), 328–332.

Regard, V., Saillard, M., Martinod, J., Audin, L., Carretier, S., Pedoja, K., Riquelme, R., Paredes, P., & Hérail, G. (2010). Renewed uplift of the Central Andes Forearc revealed by coastal evolution during the Quaternary. Earth and Planetary Science Letters, 297(1), 199–210.

Reilinger, R., McClusky, S., Vernant, P., Lawrence, S., Ergintav, S., Cakmak, R., Ozener, H., Kadirov, F., Guliev, I., Stepanyan, R., & Others. (2006). GPS constraints on continental deformation in the Africa-Arabia-Eurasia continental collision zone and implications for the dynamics of plate interactions. Journal of Geophysical Research, [Solid Earth], 111(B5). http://onlinelibrary.wiley.com/doi/10.1029/2005JB004051/full

Roberts, G. G., White, N. J., & Shaw, B. (2013). An uplift history of Crete, Greece, from inverse modeling of longitudinal river profiles. Geomorphology , 198, 177–188.

Rohling, E. J., Foster, G. L., Grant, K. M., Marino, G., Roberts, A. P., Tamisiea, M. E., & Williams, F. (2014). Sea-level and deep-sea-temperature variability over the past 5.3 million years. Nature, 508(7497), 477–482.

Rosu, A.-M., Pierrot-Deseilligny, M., Delorme, A., Binet, R., & Klinger, Y. (2015). Measurement of ground displacement from optical satellite image correlation using the free open-source software MicMac. ISPRS Journal of Photogrammetry and Remote Sensing: Official Publication of the International Society for Photogrammetry and Remote Sensing , 100, 48–59.

Rovere, A., Raymo, M. E., Mitrovica, J. X., Hearty, P. J., O'Leary, M. J., & Inglis, J. D. (2014). The Mid-Pliocene sea-level conundrum: Glacial isostasy, eustasy and dynamic topography. Earth and Planetary Science Letters, 387, 27–33.

Roveri, M., Flecker, R., Krijgsman, W., Lofi, J., Lugli, S., Manzi, V., Sierro, F. J., Bertini, A., Camerlenghi, A., De Lange, G., Govers, R., Hilgen, F. J., Hübscher, C., Meijer, P. T., & Stoica, M. (2014). The Messinian Salinity Crisis: Past and future of a great challenge for marine sciences. Marine Geology, 352, 25–58.

Royden, L. H., & Papanikolaou, D. J. (2011). Slab segmentation and late Cenozoic disruption of the Hellenic arc. Geochemistry, Geophysics, Geosystems, 12(3), Q03010.

Ruggieri, G., & d'Arpa, C. (1993). Ostracodi marini del Pliocene superiore di Altavilla (Palermo) Contributo primo. Naturalista Siciliano, S. IV, 17, 195–229.

Rupnik, E., Deseillignya, M. P., Delorme, A., & Klinger, Y. (2016). Refined satellite image orientation in the free open-source photogrammetric tools Apero/Micmac. ISPRS Annals of Photogrammetry, Remote Sensing & Spatial Information Sciences, 3(1).

Schattner, U. (2010). What triggered the early-to-mid Pleistocene tectonic transition across the entire eastern Mediterranean? Earth and Planetary Science Letters, 289(3), 539–548.

Scott, A. T., & Pinter, N. (2003). Extraction of Coastal Terraces and Shoreline-Angle Elevations from Digital Terrain Models, Santa Cruz and Anacapa Islands, California. Physical Geography, 24(4), 271–294.

Sgarrella, F., Moncharmont Zei, M., 1993. Benthic Foraminifera of the Gulf of Naples (Italy): systematics and autoecology. Boll. della Soc. Paleontol. Ital. 32, 145–264.

Shaw, B., & Jackson, J. (2010). Earthquake mechanisms and active tectonics of the Hellenic subduction zone. Geophysical Journal International, 181(2), 966–984.

Spratt, R. M., & Lisiecki, L. E. (2016). A Late Pleistocene sea level stack. Climate of the Past, 12(4), 1079.

Stirling, C. H., Esat, T. M., Lambeck, K., & McCulloch, M. T. (1998). Timing and duration of the Last Interglacial: evidence for a restricted interval of widespread coral reef growth. Earth and Planetary Science Letters, 160(3), 745–762.

Taylor, B., Weiss, J. R., Goodliffe, A. M., Sachpazi, M., Laigle, M., & Hirn, A. (2011). The structures, stratigraphy and evolution of the Gulf of Corinth rift, Greece. Geophysical Journal International, 185(3), 1189–1219.

Taymaz, T., Jackson, J., & McKenzie, D. (1991). Active tectonics of the north and central Aegean Sea. Geophysical Journal International, 106(2), 433–490.

Theodoropoulos, D. K. (1973). Physical Geography of the island of Kythira. Monograph, Athens.

van Hinsbergen, D. J. J., Hafkenscheid, E., Spakman, W., Meulenkamp, J. E., & Wortel, R. (2005). Nappe stacking resulting from subduction of oceanic and continental lithosphere below Greece. Geology, 33(4), 325–328.

van Hinsbergen, D. J. J., & Schmid, S. M. (2012). Map view restoration of Aegean–West Anatolian accretion and extension since the Eocene. Tectonics, 31(5), TC5005.

van Hinsbergen, D. J. J. Van der Meer, D. G., Zachariasse, W. J., & Meulenkamp, J. E. (2006). Deformation of western Greece during Neogene clockwise rotation and collision with Apulia. International Journal of Earth Sciences, 95(3), 463.

Willett, S., Beaumont, C., & Fullsack, P. (1993). Mechanical model for the tectonics of doubly vergent compressional orogens. Geology, 21(4), 371–374.

Zitellini, N., Ranero, C. R., Filomena Loreto, M., Ligi, M., Pastore, M., D'Oriano, F., Sallares, V., Grevemeyer, I., Moeller, S., & Prada, M. (2020). Recent inversion of the Tyrrhenian Basin. Geology, 48(2), 123–127.

AGU PUBLICATIONS

Tectonics

Supporting Information for

Quaternary E-W extension uplifts Kythira Island and segments the Hellenic Arc

G. de Gelder[1,2], D. Fernández-Blanco[2,3], N. Öğretmen[4,5], S. Liakopoulos[6], D. Papanastassiou[6], C. Faranda[5], R. Armijo[2], and R. Lacassin[2]

[1]ISTerre, Université Grenoble-Alpes, 1381 Rue de la Piscine, 38400 St. Martin d'Hères, France

[2]Université de Paris, Institut de physique du globe de Paris, CNRS, F-75005 Paris, France

[3]Barcelona Center for Subsurface Imaging, Passeig Marítim de Barceloneta 37-49, E-08003 Barcelona, Spain

[4]Eurasia Institute of Earth Sciences, Istanbul Technical University, 34467, Istanbul, Turkey

[5]Dipartimento di Scienze, Università degli Studi Roma Tre, Largo San Leonardo Murialdo, 1, 00146 Rome, Italy

[6]Institute of Geodynamics, National Observatory of Athens, GR-11810 Athens, Greece

Contents of this file

Additional Supporting Information (Files uploaded separately)

We share a georeferenced hillshade image and slope map of the 2 m-resolution Digital Surface Model through these links: https://doi.org/10.6084/m9.figshare.18715535.v1 (hillshade image) and https://doi.org/10.6084/m9.figshare.18714914.v1 (slope map). The map of Figure 2 can be downloaded in georeferenced format (as Geospatial PDF) at https://doi.org/10.6084/m9.figshare.18703496.v1.

Introduction

Figure S1 is a comparison between Digital Surface Models produced with ASTER or Pleiades imagery (as in this study). Figure S2 shows some Scanning Electron Microscope images for some of the microfossils used in the biostratigraphic dating section. Figure S3 shows sensitivity tests of the landscape evolution modeling. Figure S4 are detailed topographic cross-sections used to determine shoreline angles of marine terraces. Table S1 lists all microfossils found in the samples, and Table S2 the model parameters used for the landscape evolution modeling.

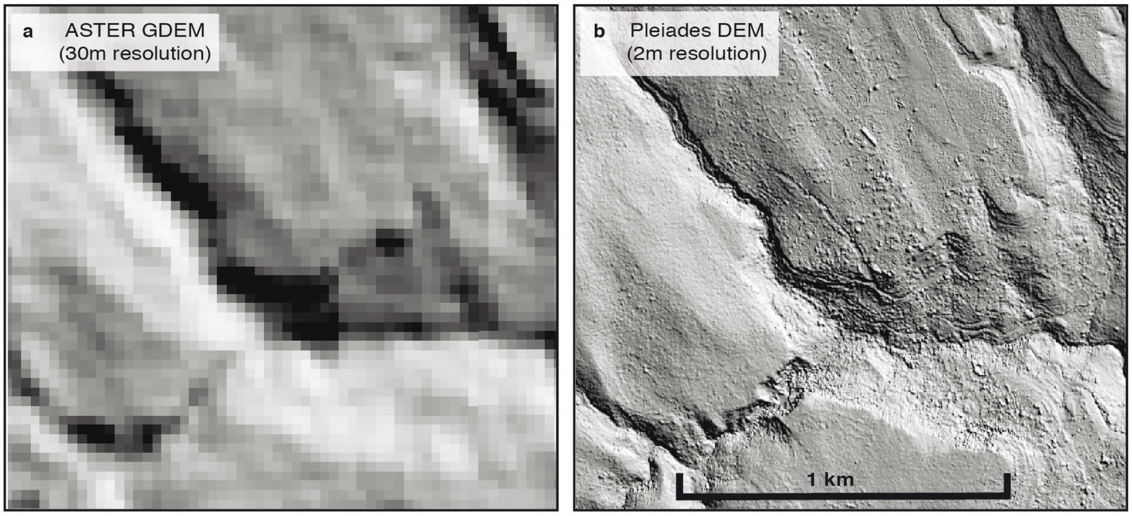

Figure S1. Topographic data comparison. Comparison between the standard Aster GDEM (30m horizontal resolution) and the DSM (2m horizontal resolution) we produced with images of the Pleiades satellite; location given by inset in Fig. 2.

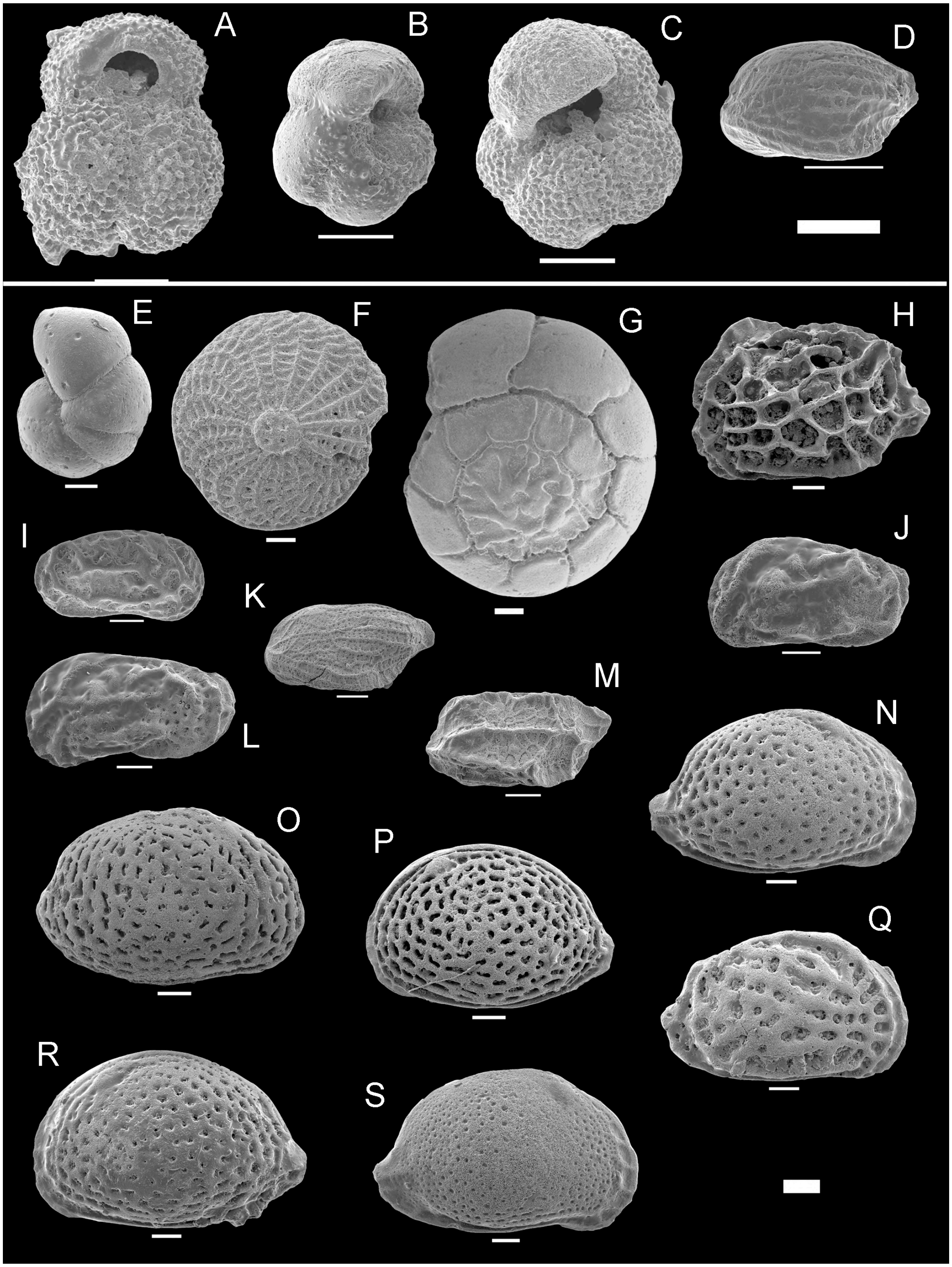

Figure S2. SEM pictures of selected planktic and benthic foraminifers and ostracods collected in the shallow marine deposits in Kythira. A. *Globigerinoides ruber*, sample Na; B.

Globorotalia crassaformis, sample Na; C. *Neogloboquadrina atlantica atlantica*, sample Na; D. *Semicytherura inversa*, sample Na; E. *Lobatula lobatula*, sample Gp; F. *Elphidium crispum*, sample Ta; G. *Aubignyana perlucida*, sample Ta; H. *Mutilus elegantulus*, sample Ta; I. *Callistocythere flavidofusca*, sample Na; J, *Callistocythere parallela*, sample Ta; K., *Semicytherura velata*, sample Ta; L. *Callistocythere intricatoides*, sample Ta; M. *Semicytherura* sp., sample Ta; N. *Aurila punctata*, sample Ta; O. *Aurila cephalonica*, sample Gp; P. *Aurila* sp., sample Ta; Q. *Cimbaurila cimbaeformis*, sample Ta; R. *Aurila anguisfoveata*, sample Ta; S. *Aurila hesperiae*, sample Ta. White bars correspond to 0.1 mm.

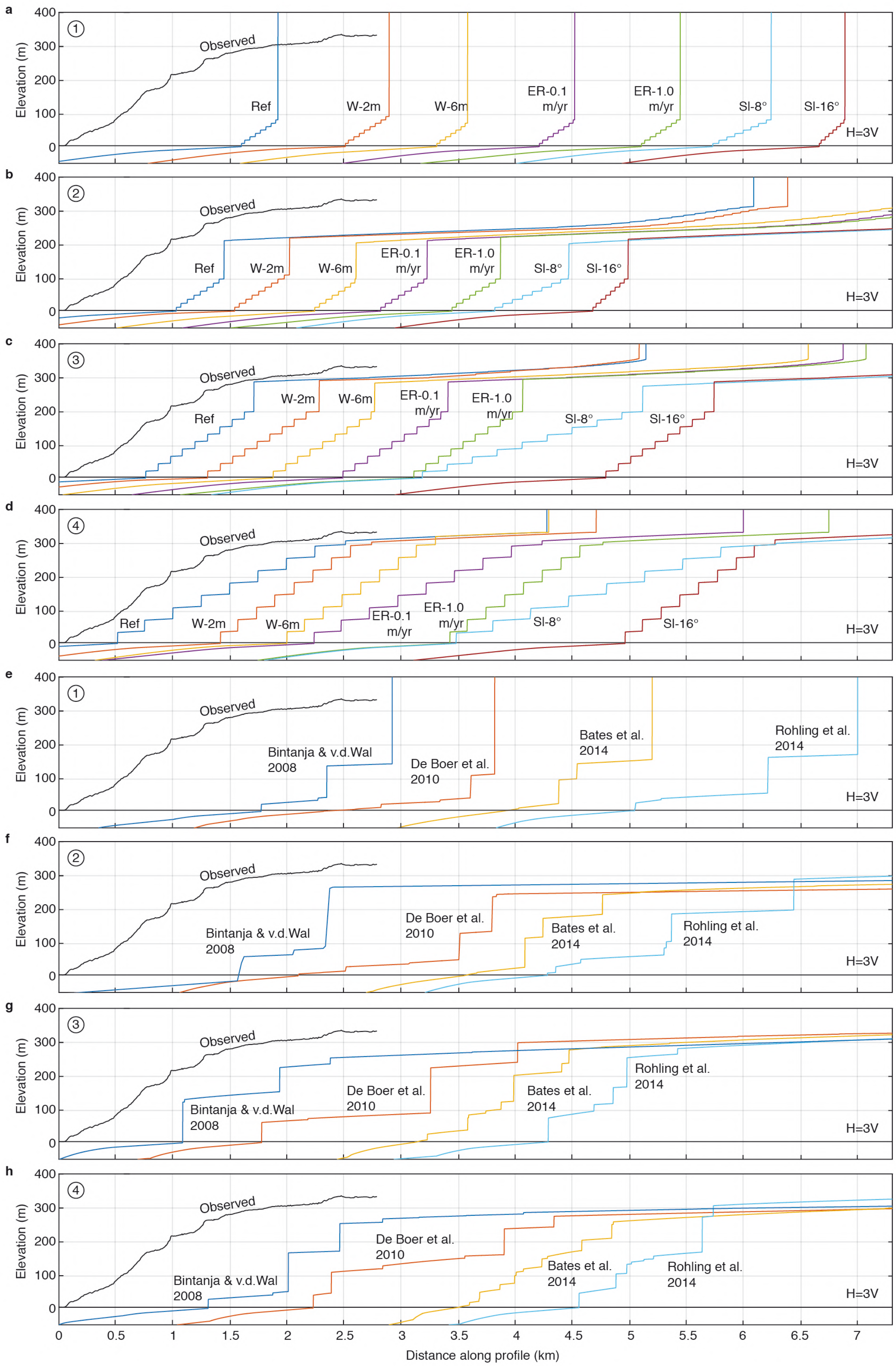

a
b
c
d
e
f
g
h
Elevation (m)
Observed
Ref
W-2m
W-6m
ER-0.1 m/yr
ER-1.0 m/yr
Sl-8°
Sl-16°
H=3V
Bintanja & v.d.Wal 2008
De Boer et al. 2010
Bates et al. 2014
Rohling et al. 2014
Distance along profile (km)

Figure S3. Sensitivity tests for LEM modeling. (a-d) Testing the influence of wave depth, erosion rate and initial slope within reasonable ranges on the 4 tested uplift rate scenarios of Fig. 9. (e-h) Using the Bintanja and van der Wal (2008), De Boer et al. (2010), Bates et al. (2014) and Rohling et al. (2014) sea-level curves (as in De Gelder et al., 2020) on the 4 tested uplift rate scenarios, with the same reference parameter values as in Fig. 9 (also see Supplementary Table 2). As the Bintanja and van der Wal (2008) only spans 3 Ma, values for the 4-3 Ma period have been copied from the De Boer et al. (2010) sea-level curve, which was derived with a similar methodology.

Figure S4 is 15 pages and can be found through:
https://doi.org/10.6084/m9.figshare.18986210.v1

Figure S4. Swath profiles used to determine shoreline angles. Map gives locations and numbering of swath profiles on a slope-map of the Pleiades DSM, and the average determined shoreline angles (dots). Color-code for the marine terraces is the same as in Fig. 8. Profiles show maximum and minimum topography, selected points on the terrace and paleo-cliff, and estimated shoreline angle elevation for two end-member scenarios: a most landward and a most seaward position of the hypothetical paleo sea-clifff.

Sample BC (2.87 – 2.59 Ma)

BC Benthic foraminifera

*Asterigerinata planorbis (*d'Orbigny, 1826)
Astrononion stelligerum (d'Orbigny, 1839)
Cibicides refulgens (de Montfort, 1808)
Cibicidoides pseudungerianus (Cushman, 1922)
Elphidium complanatum (d'Orbigny, 1839)
Elphidium crispum (Linnaeus, 1758)
Elphidium macellum (Fichtel & Moll, 1798)
Lobatula lobatula (Walker & Jacob, 1798)
Melonis soldanii (d'Orbigny, 1846)
*Uvigerina pygmaea (*d'Orbigny, 1826)

BC Ostracods

Aurila anguisfoveata (Uliczny, 1969)
Aurila cephalonica (Mostafawi & Matze-Kasarsz, 2006)
Aurila convexa (Baird, 1850)
Bairdia sp.
Buntonia conularis (Terquem, 1878)
Callistocythere intricatoides (Ruggieri, 1953)
Callistocythere parallela (Aruta, 1986)
Carinocythereis whitei (Baird, 1850)
Costa edwardsii (Roemer, 1838)
Cystacythereis rubra (Müller, 1894)
Cytherella sp.
Cytheretta subradiosa (Roemer, 1838)

Cytheropteron sp.
Echinocythereis pustulata (Namias, 1900)
Eucytherura patercoli (Mistretta, 1967)
Graptocythere intricata (Terquem, 1878)
Hemicytherura gracilicosta (Ruggieri, 1953)
Loxoconcha ovulata (Costa, 1863)

Mutilus elegantulus (Ruggieri & Sylvester-Bradley, 1875)
Paracytheridea sp.
Ruggieria sp.
Semicytherura inversa (Seguenza, 1880)
Semicytherura velata (Ciampo, 1985)
Semicytherura sp. 1
Semicytherura sp. 2
Semicytherura sp. 3
Urocythereis exedata (Uliczny, 1969)
Xestoleberis communis (Müller, 1891)

Sample GP (3.81 – 2.59 Ma)

GP Benthic foraminifera

Asterigerinata planorbis (d'Orbigny, 1826)
Cibicides refulgens (de Montfort, 1808)

GP Ostracods

Aurila anguisfoveata (Uliczny, 1969)
Bairdia sp.
Callistocythere flavidofusca (Ruggieri, 1950)
Carinocythereis whitei (Baird, 1850)
Caudites calceolatus (Costa, 1853)
Celtia quadridentata cephalonica (Uliczny, 1969)
Cystacythereis sp.
Cytheretta subradiosa (Roemer, 1838)
Eucytherura patercoli (Mistretta, 1967)
Hemicytherura gracilicosta (Ruggieri, 1953)
Loxoconcha ovulata (Costa, 1863)
Pontocythere turbida (Müller, 1894)
Ruggieria sp.
Sagmatocythere versicolor (Müller, 1894)
Semicytherura velata (Ciampo, 1985)
Tenedocythere exornata (Terquem, 1878)

Urocythereis exedata (Uliczny, 1969)
Urocythereis sp.

Sample NA (2.87 – 2.42 Ma)

NA Planktonic foraminifera

Globigerina bulloides (d'Orbigny, 1826)
*Globigerina falconensis (*Blow, 1959)
Globigerinella pseudobesa (Salvatorini, 1956)
Globigerinita parkerae (Loeblich & Tappan, 1957)
Globigerinoides elongatus (d'Orbigny, 1839)
Gobigerinoides extremus (Bolli, 1957)
Globigerinoides obliquus (Bolli, 1957)
Globigerinoides ruber (d'Orbigny, 1839)
Globigerinoides trilobus (Reuss, 1850)
Globorotalia crassaformis (Galloway & Wissler, 1927)
*Neogloboquadrina atlantica atlantica (*Berggren, 1972)
Neogloboquadrina sp.

NA Benthic foraminifera

*Amphycorina scalaris (*Batsch, 1791)
Asterigerinata planorbis (d'Orbigny, 1826)
Brizalina catanensis (Seguenza, 1862)
Brizalina dilatata (Reuss, 1850)
Brizalina sp.
Cancris oblongus (Williamson, 1858)
Cibicidoides pseudungerianus (Cushman, 1922)
Elphidium aculeatum (d'Orbigny, 1846)
Elphidium advenum (Cushman, 1922)
Elphidium macellum (Fichtel & Moll, 1798)
Lenticulina orbicularis (d'Orbigny, 1826)
Lobatula lobatula (Walker & Jacob, 1798)

Elphidium crispum (Linnaeus, 1758)
Lobatula lobatula (Walker & Jacob, 1798)
Melonis soldanii (d'Orbigny, 1846)
Planulina ariminensis (d'Orbigny, 1826)
Pleurostomella alternans (Schwager, 1866)
Sphaeroidina bulloides (d'Orbigny, 1826)

*Uvigerina peregrina (*Cushman, 1923)
Uvigerina proboscidea (Schwager, 1866)

NA Ostracods

Aurila hesperiae (Ruggieri, 1975)
Aurila punctata (von Munster, 1830)
Bairdia sp.
Callistocythere flavidofusca (Ruggieri, 1950)
Callistocythere parallela (Aruta, 1986)
Carinocythereis whitei (Baird, 1850)
Costa sp.
Cystacythereis sp.
Cytherella sp.
Echinocythereis pustulata (Namias, 1900)
Eucytherura patercoli (Mistretta, 1967)
Graptocythere intricata (Terquem, 1878)
Hemicytherura gracilicosta (Ruggieri, 1953)
Loxoconcha ovulata (Costa, 1863)
Mutilus elegantulus (Ruggieri & Sylvester-Bradley, 1875)
Parakrithe sp.
Puloniella hellenica (Mostafawi, 1989)
Pontocythere turbida (Müller, 1894)
Ruggieria sp.
Semicytherura inversa (Seguenza, 1880)
Semicytherura velata (Ciampo, 1985)
Semicytherura sp. 1
Tenedocythere sp.
Urocythereis sp.
Xestoleberis communis (Müller, 1891)

Sample QU (3.81 – 2.59 Ma)

QU Ostracods

Aurila cephalonica (Mostafawi & Matze-Kasarsz, 2006)
Aurila convexa (Baird, 1850)
Aurila hesperiae (Ruggieri, 1975)
Bairdia sp.
Callistocythere intricatoides (Ruggieri, 1953)
Callistocythere flavidofusca (Ruggieri, 1950)
Carinocythereis whitei (Baird, 1850)
Cystacythereis rubra (Müller, 1894)
Cytheretta subradiosa (Roemer, 1838)
Hemicytherura gracilicosta (Ruggieri, 1953)
Loxoconcha ovulata (Costa, 1863)

Semicytherura inversa (Seguenza, 1880)
Semicytherura velata (Ciampo, 1985)
Tenedocythere exornata (Terquem, 1878)
Urocythereis exedata (Uliczny, 1969)
Xestoleberis communis Müller, 1891

Sample TA (2.87 – 2.59 Ma)

TA Benthic foraminifera

Aubignyna perlucida (Heron-Allen & Earland, 1913)
Brizalina arta (MacFadyen, 1931)
Cibicidoides pseudungerianus (Cushman, 1922)
Elphidium crispum (Linnaeus, 1758)
Lobatula lobatula (Walker & Jacob, 1798)
Melonis soldanii (d'Orbigny, 1846)
Neoconorbina terquemi (Rzehak, 1888)
Pleurostomella alternans
Uvigerina peregrina Cushman, 1923

TA Ostracods

Aurila anguisfoveata Uliczny, 1969
Aurila hesperiae Ruggieri, 1975
Aurila punctata (von Munster, 1830)
Aurila sp. 1
Bairdia sp.
Buntonia conularis (Terquem, 1878)
Callistocythere intricatoides (Ruggieri, 1953)
Callistocythere parallela Aruta, 1986
Callistocythere sp.
Carinocythereis whitei (Baird, 1850)
Cimbaurila cimbaeformis (Seguenza, 1883)
Cymbaurila venetiensis (Uliczny, 1969)
Costa punctatissima Ruggieri, 1962
Cystacythereis rubra (Müller, 1894)
Cytherella sp.
Echinocythereis pustulata (Namias, 1900)
Loxoconcha ovulata (Costa, 1863)
Mutilus elegantulus Ruggieri & Sylvester-Bradley, 1875
Puloniella hellenica Mostafawi, 1989
Sagmatocythere cf. *S. napoliana* (Puri, 1963)
Semicytherura inversa (Seguenza, 1880)
Semicytherura velata Ciampo, 1985
Semicytherura sp. 1
Semicytherura sp. 2

Mutilus elegantulus (Ruggieri & Sylvester-Bradley, 1875)	*Tenedocythere exornata* (Terquem, 1878)
Paracytheridea sp.	*Urocythereis exedata* Uliczny, 1969
Pontocythere turbida (Müller, 1894)	*Urocythereis* sp.
Sagmatocythere versicolor (Müller, 1894)	*Xestoleberis communis* Müller, 1891

Table S1. Micropaleontology. List of all the identified species in the analyzed samples from Kythira

Parameter	Value			
Dx (m)	2			
Dt (yr)	50			
Wave Height (m)	4			
Erosion Rate (m/yr)	0.5			
Slope (degree)	12			
Scenario 1 Age (ka)	2300	2005	2000	0
Scenario 1 UR (mm/yr)	2.0	2.0	0.1	0.1
Scenario 2 Age (ka)	4000	2605	2600	0
Scenario 2 UR (mm/yr)	-0.1	0	0.12	0.12
Scenario 3 Age (ka)	4000	1505	1500	0
Scenario 3 UR (mm/yr)	-0.05	0.05	0.22	0.22
Scenario 4 Age (ka)	4000	905	900	0
Scenario 4 UR (mm/yr)	0	0	0.37	0.37

Table S2. Model parameters. Values used for the landscape evolution modeling analysis presented in Fig. 9 and described in section 5.2. Landscape evolution modeling was done using TerraceM-2 (Jara-Muñoz et al., 2019). Sensitivity tests with wave heights of 2 and 6 m, erosion rates of 0.1 and 1.0 m/yr, and slopes of 6° and 18° are given in Supplementary Figure 3